Free Energy Analysis of Peptide-Induced Pore Formation in Lipid Membranes by Bridging Atomistic and Coarse-Grained Simulations

Joshua D. Richardson[1] and Reid C. Van Lehn[1,2,*]

[1]Department of Chemical and Biological Engineering, University of Wisconsin – Madison, Madison, WI, 53706, USA.

[2]Department of Chemistry, University of Wisconsin – Madison, Madison, WI, 53706, USA.

*address correspondence to: vanlehn@wisc.edu

Abstract

Antimicrobial peptides (AMPs) are attractive materials for combating the antimicrobial resistance crisis because they can kill target microbes by directly disrupting cell membranes. Although thousands of AMPs have been discovered, their molecular mechanisms of action are still poorly understood. One broad mechanism for membrane disruption is the formation of membrane-spanning hydrophilic pores which can be stabilized by AMPs. In this study, we use molecular dynamics (MD) simulations to investigate the thermodynamics of pore formation in model single-component lipid membranes in the presence of one of three AMPs: aurein 1.2, melittin and magainin 2. To overcome the general challenge of modeling long timescale membrane-related behaviors, including AMP binding, clustering, and pore formation, we develop a generalizable methodology for sampling AMP-induced pore formation. This approach involves the long equilibration of peptides around a pore created with a nucleation collective variable by performing coarse-grained simulations, then backmapping equilibrated AMP-membrane configurations to all-atom resolution. We then perform all-atom simulations to resolve free energy profiles for pore formation while accurately modeling the interplay of lipid-peptide-solvent interactions that dictate pore formation free energies. Using this approach, we quantify free energy barriers for pore formation without direct biases on peptides or whole lipids, allowing us to investigate mechanisms of pore formation for these 3 AMPs that are a consequence of unbiased peptide diffusion and clustering. Further analysis of simulation trajectories then relates variations in pore lining by AMPs, AMP-induced lipid disruptions, and salt bridges between AMPs to the observed pore formation free energies and corresponding mechanisms. This methodology and mechanistic analysis have the potential to generalize beyond the AMPs in this study to improve our understanding of pore formation by AMPs and related antimicrobial materials.

Introduction

A pressing issue in society today is the rise of antimicrobial resistance to currently available drugs due to overprescription and overuse.[1] Microbes have a variety of mechanisms to decrease the efficacy of antimicrobial drugs, including thick biofilm matrices that restrict diffusional transport,[2, 3] mutations in target enzymes to prevent drug binding,[4] and transporter proteins (efflux pumps) that expel drugs into the extracellular environment.[5] As a result, there is significant interest in developing antimicrobial peptides (AMPs) that function via membrane disruption and are less likely to lead to resistance.[6] Naturally occurring AMPs are α-helical and typically cationic peptides that are present in the immune systems of plants and animals and contribute to their defense against foreign pathogens.[7] Their mechanism of action is generally understood as first involving the binding of AMPs to microbial membranes due to attractive electrostatic interactions between cationic side chains and anionic lipid head groups (or other membrane components).[8] How bound AMPs then lead to membrane disruption and eventual cell death, however, is less well-understood, inhibiting the rational design of new synthetic AMPs to address limitations of proteolytic degradation and low selectivity for naturally sourced AMPs when introduced *in vivo*.[9-11]

Two broad mechanisms – pore formation and the carpet mechanism – have been proposed to explain AMP-induced membrane disruption and have been shown to depend on a variety of AMP physiochemical properties such as charge, length, hydrophobic sector, and rigidity.[12] In the carpet mechanism, a high local concentration of AMPs on the surface of a membrane leads to membrane rupture and lipid micellization.[13] The carpet mechanism is typically promoted by AMPs too short to span cell membranes as an α-helix.[14, 15] For instance, aurein 1.2 is a 13-residue +1 charged peptide sourced from bell frogs that is believed to disrupt membranes via the carpet mechanism as supported by dye leakage experiments from unilamellar vesicles.[16] In the pore formation mechanism, AMPs stabilize membrane-spanning pores that compromise the membrane's ability to regulate transport. Melittin, a 26-residue +6 charged peptide that is the major component of bee venom,[17 ,18] is an example of an AMP believed to disrupt membranes via pore formation as supported by x-ray diffraction[19] and calcein leakage experiments.[20] Pore formation can be further sub-divided into two separate mechanisms: the barrel-stave mechanism, in which peptides completely line the walls of the pore to minimize lipid disruption, and the toroidal pore mechanism, in which a combination of peptides and lipid head groups line the pore. The barrel-stave model is favored by AMPs that are rigid, membrane-spanning, and have a high hydrophobic content to mediate both peptide-peptide and peptide-lipid interactions while excluding lipid headgroups from the aqueous pore,[21 ,22 ,23] whereas the toroidal model allows for more flexibility in AMP structure (such as proline and glycine 'kinks' in the α-helix that reduce rigidity[21,24, 25]) because lipids deform such that their head groups line the pore and interact with peptides.

Although experiments can provide insight into the preference of AMPs to disrupt membranes by either the carpet mechanism or pore formation, it remains difficult to gain molecular-scale insight into peptide-lipid interactions that dictate the thermodynamics of these processes or distinguish between the barrel-stave and toroidal pore models. To corroborate experimental data, molecular dynamics (MD) simulations have been used to resolve mechanistic pathways for peptide-membrane interactions, including pore formation.[22, 25-34] Theory and simulation studies suggest that long-lived metastable pores form in membranes once a critical pore radius is reached, which requires the system to overcome a free energy penalty associated with unfavorable water-lipid tail interactions or lipid bending at the pore edge.[28, 32] Therefore, variations in this free energy due to the addition of AMPs can resolve whether pore formation mechanisms are favorable.

A robust enhanced sampling method that has been applied for studying pore formation in bilayers is umbrella sampling, which permits a potential of mean force (PMF) to be calculated as a function of a pre-defined collective variable (CV) that is biased across an interval of interest.[35] Harmonic biasing potentials are applied along this CV to sample a large range of system configurations and then energetic free energy barriers and metastable states can be determined with the weighted histogram analysis method (WHAM).[36] Umbrella sampling requires the selection of an appropriate CV, however, to ensure that the sampled PMF is physically relevant. Tolpekina, et al. proposed an early CV (which we refer to as the tanh CV) to study the free energy of pore formation in bilayers with MD simulations. The tanh CV is calculated using a hyperbolic tangent function applied to the lateral distance of lipid tails which increases when lipid tails atoms are farther from a pre-defined pore center.[37] Recently, the tanh CV has been used with umbrella sampling to study the energetics of pore formation in 18 different lipid membrane compositions in the presence of cationic cyclic nonaarginine peptides with coarse-grained simulations[38] and fully atomistic POPC membranes with an increasing number of melittin peptides.[28] In the latter case, metastable free energy minima were resolved with 4 or more melittin peptides lining a toroidal transmembrane pore, which could imply a long-lived pore that would eventually lead to cytotoxicity. This observation, however, required the orientation of peptides to be hand-selected *a priori* on the outer leaflet of the membrane, mainly due to slow diffusional limitations of peptides relative to the membrane in umbrella sampling.[28]

Despite its promise, a limitation of the tanh CV is that it exhibits large hysteresis during umbrella sampling depending upon initial system configurations, suggesting that the pore formation process is not fully captured through a bias applied to lipid tail groups only.[39] To address this issue, Hub and Awasthi developed a pore nucleation CV (referred to as ξ) that captures pore formation by biasing both water molecules and lipid headgroups.[40] The value of ξ is determined by first defining a transmembrane cylinder of set radius that spans the lipid bilayer and is divided into horizontal slices, and then calculating the occupancy of slices by oxygen atoms in lipid head groups and water molecules; ξ increases in value with increased occupancy, which occurs when either lipid head groups or water molecules span the bilayer to form a hydrophilic pore.[40] A typical PMF predicted with ξ has a minimum for an unperturbed membrane around $\xi = 0.2$, a maximum due to the formation of a continuous polar defect (nucleation) when $\xi > 0.7$, and a local minimum at $\xi = 1.0$ for a fully nucleated pore. ξ has been shown to be hysteresis-free and quickly converge in umbrella sampling simulations of pore formation in pure membranes[40,41] and in simulations of pore formation stabilized by drugs[42] and polycations.[43] Nonetheless, ξ has yet to be applied in membranes in the presence of AMPs, which may be due to the long-timescale lateral diffusion of peptides during pore lining[28, 44] required to resolve physically relevant free energy profiles.

In this study, we utilize umbrella sampling simulations as a function of ξ to study membrane pore formation in the presence of different AMPs with the goal of resolving corresponding free energy profiles and observing cooperative peptide aggregation and pore lining. To address the challenge of long-timescale AMP diffusion, we first nucleate aqueous pores in a model DMPC membrane using the MARTINI coarse-grained force field, then apply a backmapping procedure to obtain fully atomistic system representations that better capture the interplay of lipid-AMP-water interactions during pore formation. Using melittin as a model pore former and aurein 1.2 as a non-pore former, we calculate the free energy barrier for pore formation in the presence of these peptides and show that melittin preferentially forms toroidal-like pores in membranes by significantly decreasing the energy barrier required for pore nucleation relative to pure DMPC. To further test the robustness of this methodology, we model the 23-residue +3 charged AMP magainin 2 to compare its propensity for pore formation to aurein 1.2, melittin, and previous MD studies.[25,45] Analysis of bilayer structural perturbations and peptide-peptide interactions provide insight into variations in pore formation free energies for these three peptides. Overall, we find that this methodology can be utilized to mechanistically support pore formation affinities of AMPs of varying physiochemical properties (e.g., length, charge, hydrophobicity) previously reported in the literature, and expect that this approach may further be applied to understand the behavior of new AMP structures discovered as part of ongoing efforts to combat the antimicrobial resistance crisis.

Methods

System Preparation and Coarse-Grained Simulation Parameters

Four different coarse-grained (CG) simulation systems were modeled with the MARTINI 2.2 forcefield[46] to test the influence of AMPs on pore formation. The four systems all included a bilayer containing 288 DMPC lipids and with either zero peptides (Pure DMPC), 8 aurein 1.2 (8 AUR) peptides, 8 melittin (8 MEL) peptides, or 8 magainin 2 (8 MAG) peptides. This number of peptides was chosen based on the peptide to lipid ratios observed to form fully lined melittin pores (the reference pore-forming peptide in our study); past studies have found that between 4 and 7 peptides line pores in phosphatidyl choline lipid membranes during full nucleation.[25, 28] Each system was initially built with the *insane* script.[47] Atomistic representations of each peptide were first created using Avogadro,[48] and the *martinize* script[46] was utilized to convert these to CG representations based on an average 4:1 mapping of heavy atoms to CG beads. The DMPC membrane was placed in the center of a solvated simulation box (spanning the *xy*-plane). For systems with peptides, the peptides were initialized in a 2 by 4 grid located 2.5 nm above the *z* center of mass (COM) of the membrane. Each system was solvated with at least 10 MARTINI W beads (representing 40 water molecules) per lipid molecule to prevent inter-bilayer interactions in the *z* direction across the simulation periodic boundaries and to match prior simulations of pore nucleation.[40] Additionally, chloride counterions were added to neutralize peptide-containing systems. Table 1 shows a summary of these systems and components.

Table 1: Summary of systems modeled in coarse-grained (MARTINI) and all-atom (CHARMM36) molecular dynamics simulations.

	Pure DMPC	8 AUR	8 MEL	8 MAG
Peptides	None	8 Aurein 1.2	8 Melittin	8 Magainin 2
DMPC Lipids	288	288	288	288
CG Water beads (W)	2888	3375	2939	2980
AA Water molecules (TIP3P)	11552	13532	11948	12016
Chloride (Cl-)	0	8	48	24

All MD simulations were conducted using Gromacs 2021.5 patched with PLUMED 2.8[49]. Energy minimization used the steepest descent algorithm with a maximum step size of 0.01 nm and tolerance of 100 kJ mol^{-1} nm^{-1}. A 2-step equilibration process was implemented to ensure peptide binding to the upper leaflet of the DMPC membrane (as visualized in Figure S1). In the first step, peptides were permitted to equilibrate in MD simulations in which a bias was applied using the PLUMED upper walls approach between the COM of each peptide and the membrane in the *z* direction to prevent peptides from diffusing into solution away from the membrane. In addition, 1000 kJ/mol harmonic restraints were placed on the *x* and *y* positions of backbone termini beads (Figure S1b). This equilibration step promotes peptide rotation and electrostatic binding to DMPC while maintaining the initial grid-like setup (Figure S1a) and preventing peptide aggregation in solution because the goal of this study is to observe collective aggregation of peptides as a consequence of diffusion at the membrane surface. In the second step, the system was further equilibrated without any bias applied to allow for the natural clustering and lateral diffusion of peptides on the membrane (Figure S1c). Both equilibration steps were performed for 50 ns with a timestep of 0.02 ps.

All CG simulations were performed at a temperature of 323 K. This temperature was chosen because the freezing temperature is as high as 300 K for MARTINI water beads represented with P4 particles[50]; moreover, this temperature permits comparison to free energy profiles from prior literature results utilizing the ξ CV at 323 K.[40] While alternative versions of the MARTINI force field more accurately treat electrostatic interactions to eliminate the unphysical freezing of MARTINI beads,[51, 52] MARTINI 2.2 was adequate for our study by permitting the computationally efficient binding of peptides to DMPC membranes and capturing lipid structural deformations important to the pore formation process that are not expected to be driven by electrostatic interactions. Moreover, the primary goal of the CG simulations was to generate reasonable atomistic configurations after following the backmapping procedure described below. The Verlet cutoff scheme was implemented for neighbor searching with a buffer tolerance of 0.005 kJ mol^{-1} ps^{-1}. Lennard Jones interactions were cut off at a distance of 1.1 nm, and electrostatic interactions were calculated with the particle mesh Ewald (PME) method with a short-range cutoff of 1.1 nm.[53] A velocity-rescale thermostat[54] was used to control the temperature at 323 K with a time constant of 1 ps and the Berendsen barostat[55] controlled the pressure at 1 bar with a semi-isotropic pressure coupling scheme with 3×10^{-4} bar^{-1} compressibility and a 5 ps time constant. The system dielectric constant was set to 15 as recommended for the MARTINI 2.2 force field.[50]

Backmapping Coarse-Grained Systems to All-Atom Representations

CG systems were backmapped to all-atom (AA) representations compatible with the CHARMM36 force field using an implementation of the *backward* tool.[56] AMP amino acid sequences along with CG and AA representations are shown in Figure 1a-c, and corresponding helical wheel representations for all AMPs are shown in Figure S3. Each system was energy minimized using a two-step approach as recommended by the initial implementation of *backward*[56]. First, all peptide-peptide and membrane-membrane nonbonded interactions were set to zero and the group cutoff scheme was implemented to resolve atomic clashes and overlap from backmapping. Second, all nonbonded interactions set to their standard values for the CHARMM36 force field and the Verlet cutoff scheme was used. Both energy minimization steps implemented the steepest descent algorithm with a maximum step size of 0.1 nm and tolerance of 1000 kJ mol^{-1} nm^{-1} for a maximum of 1000 steps.

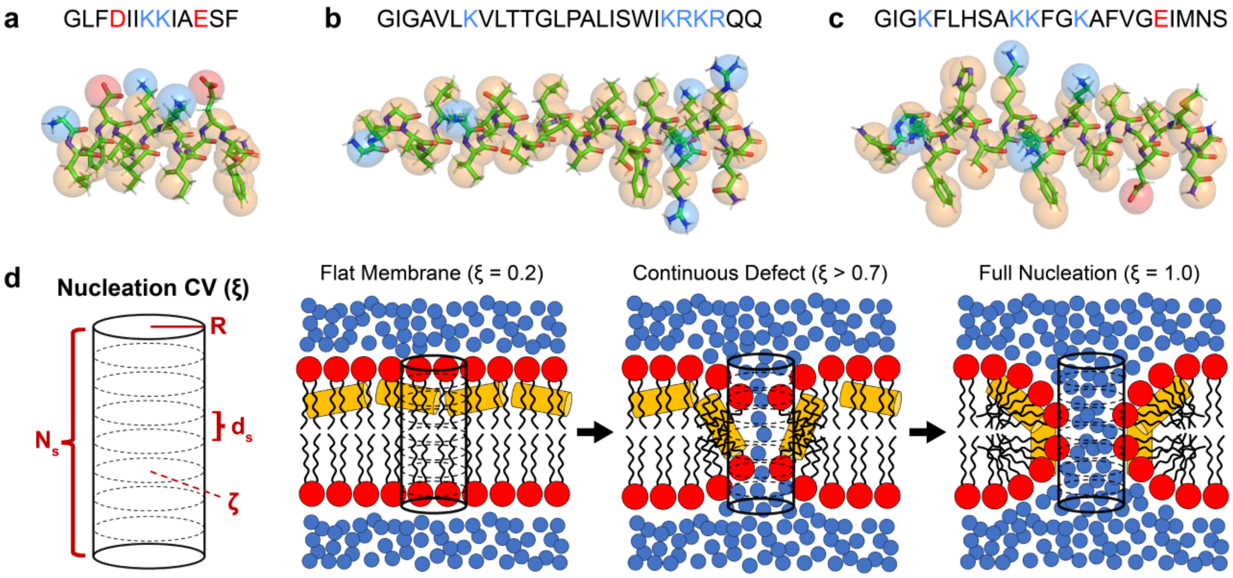

Figure 1: All-atom to coarse-grained mapping representation and amino acid sequence for each of the antimicrobial peptides studied: (a) Aurein 1.2, (b) Melittin, and (c) Magainin 2. Positively and negatively charged side chains are colored blue and red respectively. Additionally, the protonated N-terminus is blue for Aurein 1.2 and Melittin. (d) Schematic demonstrating nucleation CV (ξ) implementation along with representative system configurations at key ξ values for general peptide-containing (orange cylinders). DMPC systems. DMPC heads are red, peptides are orange cylinders, and water molecules as blue spheres.

Energy minimization of the AA systems was followed with 4 steps of *NVT* equilibration using timesteps of 0.0002, 0.0005, 0.001, and 0.002 ps with 1000 kJ/mol position restraints on all lipid and peptide heavy atoms for 500 steps each. The Verlet cutoff scheme was implemented for neighbor searching with a buffer tolerance of 0.005 kJ mol^{-1} ps^{-1}. Lennard-Jones interactions were implemented by smoothly switching forces to zero between 1 to 1.2 nm, and electrostatic interactions were calculated with the PME method with a short-range cutoff of 1.2 nm. A velocity-rescale thermostat was used to control the temperature at 323 K to match the CG system temperature with a time constant of 0.1 ps. After *NVT* equilibration, three 500 step *NPT* equilibration simulations were then conducted: the first with a timestep of 0.001 ps and 1000 kJ/mol heavy atom position restraints, then with a timestep of 0.002 ps and 1000 kJ/mol heavy atom position restraints, and finally with a timestep of 0.002 ps and no restraints. The Berendsen barostat was implemented to control the pressure at 1 bar using a semi-isotropic pressure coupling scheme with a 4.5×10^{-5} bar^{-1} compressibility and a 5 ps time constant. All other parameters were identical to *NVT* equilibration. The final configurations obtained from the backmapping and AA system equilibration were then used for further umbrella sampling calculations as detailed below.

Implementation of Nucleation Collective Variable

To bias the formation of transmembrane pores, the nucleation CV (ξ) proposed by Hub and Awasthi[40] was implemented as a collective variable in PLUMED by adapting a previous methodology used to form a fusion stalk between parallel bilayers in MARTINI.[57] As described previously,[40] ξ increases from 0 to 1 as more polar atoms occupy N_s cylinder slices each of height d_s that span a cylinder of height $N_s \times d_s$ and radius R. The cylinder height is chosen to match the thickness of the lipid membrane, including the polar head group region, as schematically shown in Figure 1d. Equation 1 defines ξ as:

$$\xi = N_s{}^{-1} \sum_{s=0}^{N_s-1} \delta_s(N_s{}^{(p)}) \tag{1}$$

In this equation, $N_s{}^{(p)}$ is the number of phosphate oxygen and water oxygen atoms in a slice s of the cylinder. The switching function δ_s is applied to $N_s{}^{(p)}$ to smoothly increase $\delta_s(N_s{}^{(p)})$ from 0 to 1 for each slice as defined in Equation 2:

$$\delta_s\left(N_s{}^{(p)}\right) = \begin{cases} \zeta \times N_s{}^{(p)} \quad , & N_s{}^{(p)} \leq 1 \\ 1 - c \times e^{-b \times N_s{}^{(p)}}, & N_s{}^{(p)} > 1 \end{cases} \tag{2}$$

ζ indicates the value of $\delta_s(N_s{}^{(p)})$ upon the addition of the first polar atom ($N_s{}^{(p)} = 1$), which exponentially approaches $\delta_s\left(N_s{}^{(p)}\right) = 1$ when 2 or more polar atoms occupy a slice ($N_s{}^{(p)} > 1$). ζ is a coefficient that is constant during the implementation of ξ and is equal to 0.75 for all simulations in this work. The other parameters are $b = \zeta/(1- \zeta)$ and $c = (1- \zeta)e^{b}$. A value of $\xi = 0.2$ corresponds to a flat, pore-free membrane, whereas a value of $\xi = 1.0$ corresponds to a fully nucleated pore with 3 or more polar atoms in each slice.[40] Figure 1d shows the parameters used to calculate ξ, along with expected behavior for a representative peptide-containing system during the evolution of ξ from 0.2 to 1.0.

For the AA systems, recommended parameters from the initial implementation of ξ for DMPC were utilized: $R = 0.8$ nm, $\zeta = 0.75$, $d_s = 0.1$ nm, and $N_s = 26$. However, to adapt ξ to CG systems, PO4 beads in DMPC (representative of phosphate groups) and W beads (representative of 4 atomistic water molecules) were counted in the implementation of ξ instead. To account for the reduced granularity of the system, the height of the cylinder slices d_s was increased from 0.1 nm to 0.2 nm, which is consistent with previous studies that implemented the nucleation CV for CG systems.[58, 59] Additionally, Figure S6 shows that trends in pore water content as a function of ξ for CG systems are in good agreement with AA systems when using this larger slice thickness. The values of R and ζ were kept as 0.8 nm and 0.75 respectively. To determine the value of N_s, unbiased simulations of the pure 288-lipid DMPC membrane system were performed for a range of values and N_s was chosen as 16 to match an average value of $\xi = 0.2$ most closely (Figure S2).

Umbrella Sampling Calculations

To prepare CG systems for umbrella sampling, starting configurations were generated by increasing ξ during a 50 ns steered MD simulation from an initial value of $\xi = 0.2$ to $\xi = 1.0$ using a harmonic potential with a force constant of 30,000 kJ mol^{-1}. A total of 23 windows were used for umbrella sampling: 11 windows from $\xi = 0.2$ to $\xi = 0.7$ with an increment of 0.05 and force constant 10,000 kJ mol^{-1} and 12 windows from $\xi = 0.725$ to $\xi = 1.0$ with an increment of 0.025 and force constant 20,000 kJ/mol^{-1}. Each window was simulated for 600 ns. The first 500 ns of each umbrella sampling trajectory was discarded to account for long timescale equilibration and diffusion of peptides around the pore. The same simulation parameters from the unbiased equilibration system preparation step ('System Preparation and Coarse-Grained Simulation Parameters' section) were adapted for these production umbrella sampling runs, except the Parrinello-Rahman barostat[60] with a 12 ns time constant was used instead of the Berendsen barostat. Simulation configurations were saved every 0.1 ns for analysis.

For AA systems, final configurations from the 500 ns CG equilibration simulations were backmapped to AA resolution (as described above in the 'Backmapping Coarse-Grained Systems to All-Atom Representations' section) and used as starting configurations for umbrella sampling, using the same number of windows and ξ spacing as CG systems. A force constant of 5,000 kJ mol^{-1} was used for the $\xi = 0.2$ to $\xi = 0.7$ windows, and a force constant of 10,000 kJ mol^{-1} was used for the $\xi = 0.7$ to $\xi = 1.0$ windows. Each window for the Pure DMPC and 8 MAG systems was simulated for 50 ns and each window for the 8 AUR and 8 MEL systems was simulated for 70 ns. The first 10 ns was discarded for equilibration. System parameters were adapted from the last *NPT* simulation for system preparation ('Backmapping Coarse-Grained Systems to All-Atom Representations' section), using the Parrinello-Rahman barostat instead of the Berendsen barostat and using either a temperature of 300 K or 323 K. Simulation configurations were saved every 0.1 ns for analysis. Potential of Mean Force (PMF) profiles were then constructed using Grossfield's implementation of the Weighted Histogram Analysis Method[61] for both the CG and AA representations of the four systems.

Results and Discussion

Coarse-Graining Increases Peptide Lateral Diffusion and Pore Lining

The goal of this study is to investigate the impact of membrane-bound peptides on the thermodynamics of pore formation, which requires simulation workflows that obtain configurations of reasonable peptide-lined pore structures. While atomistic simulations can generate physically reasonable pore formation free energies,[40] the slow lateral diffusion of membrane-bound peptides typically requires the configuration of peptides near the pore to be predetermined.[28] To overcome this challenge, we first perform CG simulations using the MARTINI 2.2 force field to accelerate lateral diffusion of membrane-bound peptides prior to eventual backmapping to enable AA simulation. Compared to AA forcefields, the smoothed energy landscape of CG simulations accelerates the dynamics of lipids and proteins relative to experimental measurements.[50, 62, 63] Faster lateral diffusion permits peptides to line pores as a consequence of long timescale natural clustering[27] at multiple ξ values. To corroborate that this approach would expedite peptide pore lining, we compared lateral diffusion coefficients (D_{lat}) computed from CG and AA simulations for DMPC lipids (from the Pure DMPC system) and for the aurein 1.2 (AUR), melittin (MEL), and magainin 2 (MAG) peptides (see Section S2 for more details). Figure S8 shows that the value of D_{lat} for DMPC from

AA simulations (19.68×10^{-12} m^2s^{-1}) is comparable to experimental measurements using pulsed field gradient NMR (20×10^{-12} m^2s^{-1})[64] while CG systems yield D_{lat} values that are 2.2 to 9.3 times larger. The lower D_{lat} for MEL (1.38×10^{-12} m^2s^{-1}) and MAG (1.56×10^{-12} m^2s^{-1}) peptides compared to AUR (3.35×10^{-12} m^2s^{-1}) can be partially explained by molecular crowding and electrostatic repulsion for these peptides because they are longer and more charged than AUR. Similar findings and rationale were previously found in atomistic simulations of the lateral diffusion of polycations adsorbed to POPC as the number of highly charged cations increased.[43]

We next determined the propensity of each peptide to line pores, and if the number of peptides lining the pore converges, during the 500 ns CG equilibration simulations that were performed for the umbrella sampling windows with CV values corresponding to the onset of pore nucleation ($\xi \geq 0.7$). For each system, we first define the pore peptide density as the peptide density within 0.5 nm in the z direction (1 nm total) of the pore center and was calculated using the *gmx density* tool by integrating the density profile of all peptide beads (in kg/m^3) from $z = -0.5$ nm to $z = 0.5$ nm. This range corresponds to the central, hydrophobic region of the membrane, and consequently only peptides in the middle of the pore contribute to the pore peptide density and no radial distance threshold relative to the pore is needed. Pore peptide densities were then divided by the density attributed to one pore-lining peptide (see Figure S10) to approximate the number of pore-lining peptides as a function of equilibration time. Figure 2 shows the average number of pore-lining peptides averaged over 5 ns intervals (trajectories saved every 0.1 ns) for windows with $\xi = 0.7, 0.85$, and 1.0. Further information and visualization on how pore peptide density is calculated are included in Section S3. Figure S4 includes additional visualization of pore structures for $\xi = 1.0$ from all three simulation trials, and additionally illustrates that during equilibration it is possible for some peptides to diffuse to the lower leaflet (through the pore).

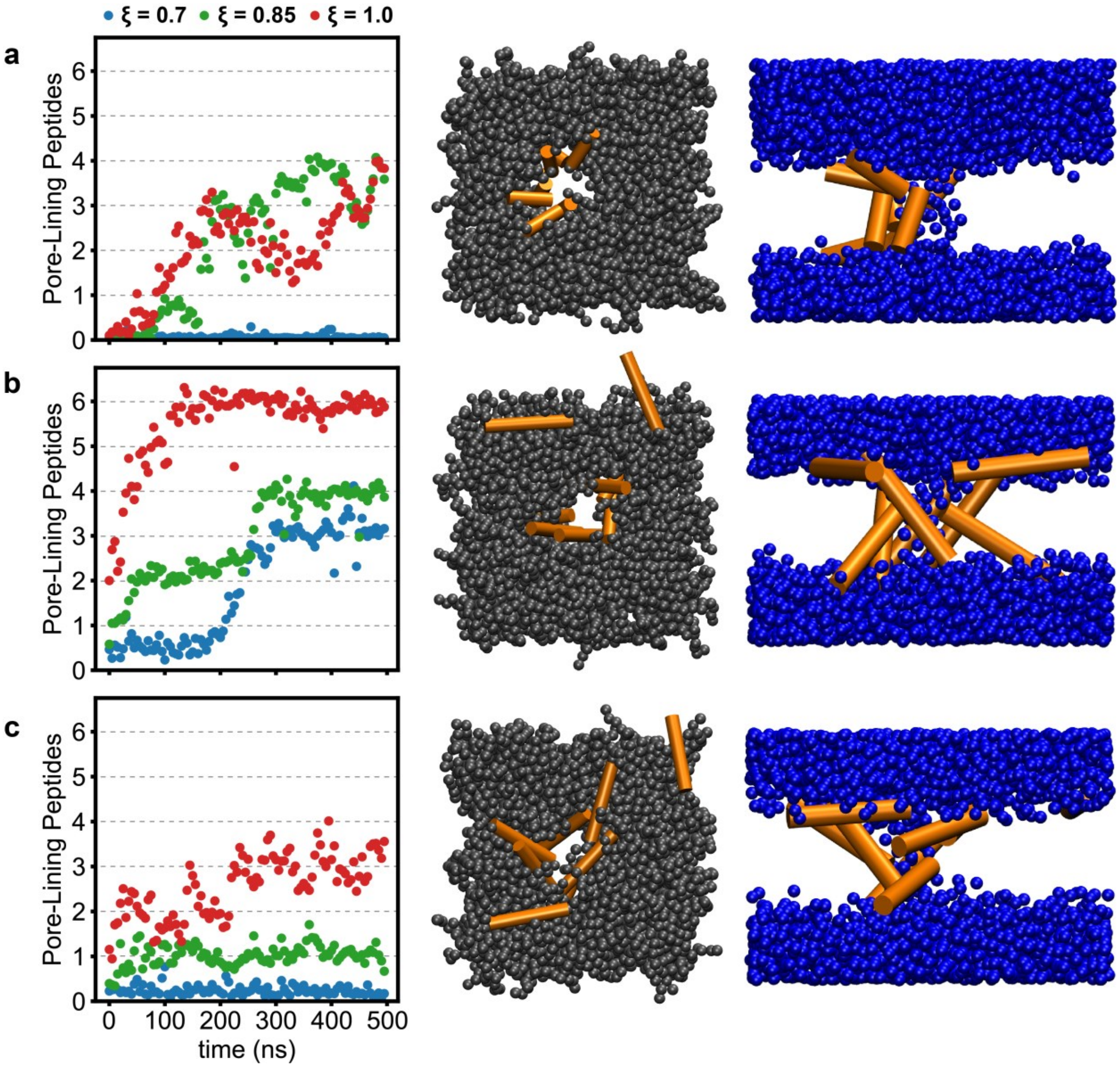

Figure 2: Analysis of peptide pore-lining during CG equilibration simulations for (a) 8 AUR, (b) 8 MEL, and (c) 8 MAG. Plots at left indicate the number of pore-lining peptides vs. simulation time for umbrella sampling windows with $\xi = 0.7$ (blue), 0.85 (green), and 1.0 (red), corresponding to the onset of pore formation. Each point reports the average number of pore-lining peptides within a 5 ns interval (see Section S3 for calculation details). Analysis of pore lining for two simulation replicates are provided in Figure S10. Simulation snapshots show the top (middle image) and side (right image) views of the last simulation configurations for the $\xi = 1.0$ window. DMPC beads are grey, peptides are orange cylinders, and water beads are blue. Water beads are omitted in the top view and DMPC beads are omitted in the side view image for visual clarity. Simulation snapshots of the pure DMPC membrane at $\xi = 0.7$, 0.85, and 1.0 are provided for reference in Figure S5.

For the AUR peptides (Figure 2a), both the $\xi = 0.85$ and 1.0 windows end with around 4 peptides lining the transmembrane pore. The number of pore-lining peptides exhibit large fluctuations throughout the simulations, and consequently it is unclear if there is a preferred number of peptides near the pore. Simulation snapshots indicate that the AUR peptides appear to line the pore on only one side in disordered structures for these ξ values. This observation could be indicative of unfavorable pore formation as supported by previous research pointing to AUR being too short to span lipid membranes as an α-helix[65, 66] and MARTINI studies that observe strong clustering behavior between AUR peptides mostly mediated by favorable hydrophobic interactions with isoleucine.[15]

Conversely, there is clear convergence after only 300 ns of equilibration for the MEL peptides in all three windows (Figure 2b), with 6 peptides lining the pore at $\xi = 1.0$. Although the peptides themselves are not directly biased when biasing ξ, during system equilibration the N-termini of the peptides are involved in pore lining while the highly charged C-termini remain in the interfacial region of the membrane. This behavior is similar to previous unbiased coarse-grained simulations of MEL peptides in POPC membranes, where a star-like configuration of 4 MEL peptides with their N-termini facing each other was a precursor to cooperative membrane penetration and pore formation.[67] The high positive charge due to the lack of amphiphilicity at the C-terminus of MEL (Figure 1b) is the most likely contributor to this lining behavior by MEL N-termini, preventing unfavorable interactions of hydrophobic DMPC tails with charged MEL sidechains if the C-terminus were to line the pore. Unlike AUR and MAG, MEL also preferentially lines the pore at $\xi = 0.7$, further supporting its propensity to line pores. Coupled with its relatively small molecular diameter near the N-terminus (Figure 1b), MEL has a large number of hydrophobic residues (I, L) in this region to mediate favorable interactions with lipid tails, while hydrophilic residues (K, T) face the aqueous environment.[68]

Lastly, MAG has similar pore lining tendencies to AUR, including a lack of peptides in the pore at small pore sizes ($\xi = 0.7$, Figure 2c). Approximately 3 peptides line the aqueous pore in a disordered structure while the remainder cluster on the membrane surface as visualized in the simulation snapshots shown in Figure 2c. We attribute the larger fluctuations of the converged number of pore-lining peptides for MAG compared to MEL (Figure 2) to the number of large side chains for MAG compared to MEL (Figure 1) in the mid-helix that line the pore and contribute to fluctuations in the pore peptide density. These observations suggest that a higher peptide to lipid ratio (~1/20) than studied in our simulations (1/36) may be required to promote pore lining by a larger number of MAG peptides, as supported by early MARTINI simulations of DPPC bilayers[25] as well as experimental NMR spectroscopy[69] and LUV calcein leakage[70] results. Alternatively, the relatively low number of pore-lining MAG peptides could be because the diameter of MAG is large compared to the pore radius sampled by ξ due to bulkier sidechains in the helix (e.g. K and F in Figure 1c) compared to MEL.[71, 72] Nonetheless, we note that the number of pore-lining peptides for the fully nucleated $\xi = 1.0$ state is comparable to AUR, motivating further analysis of the effect of MAG on pore nucleation.

To further support convergence of peptide configurations in the pore, we analyzed the prevalence of sidechain-sidechain interactions between peptides for the $\xi = 1.0$ window for the beginning (0-50 ns) and end (400-450 ns and 450-500 ns) of the 500 ns equilibration simulations. We summed the total number of instances where the centers of geometry for pairs of sidechains from different peptides were within 0.8 nm, and normalized them by the total number of sidechain-sidechain interactions between all peptides. Figure S11 shows heatmaps of peptide sidechain interactions as percentages of the total number of peptide sidechain interactions. AUR shows large differences in these sidechain interaction distributions when comparing the 400-450 ns and 450-500 ns trajectory blocks, reflecting the disordered pore structure described above. For AUR, pore lining is largely stabilized by strong C-terminal interactions (Figure S11a), which have been shown to be important for peptide aggregation and membrane disruption in DMPC membranes.[15] Conversely, MEL and MAG sidechain interaction profiles are stable for the last 100 ns of equilibration, further supporting convergence of the number of pore-lining peptides (Figure 2b-c) for the $\xi = 1.0$ window. Final MEL interactions are concentrated near the N-terminus due to preferential pore lining of this region (Figure S11b). Final MAG configurations appear to be largely stabilized by strong hydrogen bonding interactions such as H7-S23, K11-E19, and K11-S23 (Figure S11c), as discussed in more detail below.

Taken together, these results demonstrate that coarse-grained simulations using the ξ CV can lead to the observation of peptide-lined aqueous pores without needing to predefine peptide configurations on the membrane surface or biasing the peptide beads themselves, motivating further analysis of the thermodynamics of pore formation in the presence of peptides.

Peptides Decrease Free Energies for Pore Formation in CG Simulations

We next computed PMFs for pore formation in the presence of peptides for the CG systems. Because ξ was first developed to bias the oxygen atoms of water molecules and lipid head phosphates for the atomistic Berger and CHARMM36 force fields,[40] we performed several tests comparing PMFs for pure DMPC obtained from biasing MARTINI water beads and DMPC lipid PO4 beads to confirm sufficient membrane size, absence of hysteresis, and convergence (see section S4 for more details). These comparisons indicate that 288 lipids are sufficient to avoid finite-size artifacts (Figure S12a), initial configurations sampled from either a forward ($\xi = 0.2$ to 1.0) or backward ($\xi = 1.0$ to 0.2) steered molecular dynamics simulation lead to identical PMF profiles (Figure S12a), and PMF convergence is observed within 20 ns of sampling for each window (Figure S12b). There is also a PMF minimum near $\xi = 0.2$ which confirms proper selection of the number of slices of the membrane-spanning cylinder. These results support the choice of parameters used to apply the nucleation CV for the CG simulations.

Figure 3a shows PMFs for the Pure DMPC, 8 AUR, 8 MEL, 8 MAG systems for values of ξ ranging from 0.2 (flat membrane) to 1.0 (fully nucleated pore). Each curve is the average of three replicas that differ in the random sampling of velocities after 500 ns of equilibration, leading to unique 100 ns production simulations. Each replica is set to zero independently at its minimum value and the standard error across the 3 trials is indicated by the shaded region around each PMF. Consistent with the Pure DMPC umbrella sampling simulations, membrane systems containing 8 peptides (AUR, MEL, or MAG) embedded in the upper leaflet also demonstrate a free energy minimum at $\xi \approx 0.2$, and there is sufficient convergence after only 40 ns of umbrella sampling for each system (Figure S13).

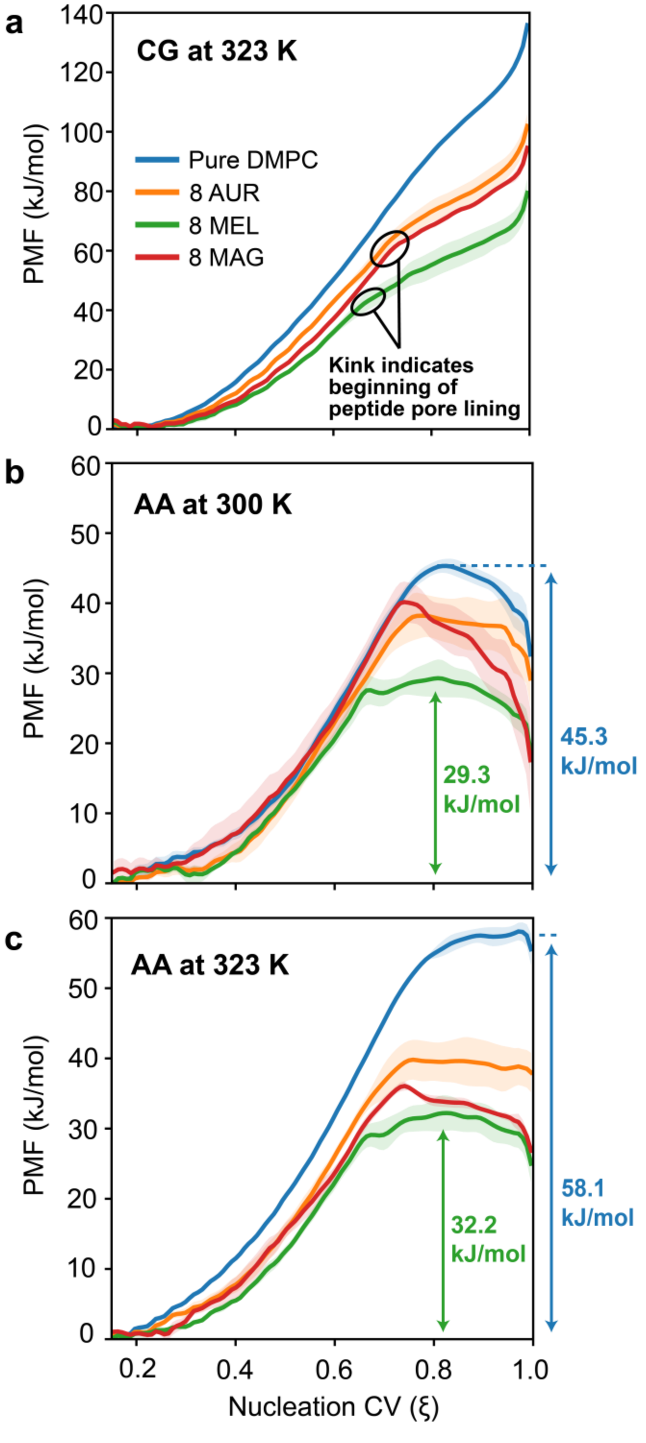

Figure 3: PMF profiles for (a) CG systems at 323 K, (b) AA systems at 300 K, and (c) AA systems at 323 K. Shaded regions indicate the standard error from 3 replicate umbrella sampling trials. PMFs were computed using WHAM with 100 bins from $\xi = 0.12$ to $\xi = 1.0$. The onset of pore lining by peptides corresponds to kinks in the CG PMF profiles for the 8 AUR, 8 MEL, and 8 MAG as captioned in (a). Pore formation barriers (in kJ/mol) are reported for AA systems (b-c) on each plot for pure DMPC (blue) and 8 MEL (green) systems. Convergence analyses for all PMF profiles are provided in Figure S13-S15.

Previous studies implementing ξ with all-atom force fields have observed nonmonotonic PMF that exhibit maxima coinciding with pore nucleation at approximately ξ = 0.7 – 0.9 followed by minima at ξ = 1.0, which is consistent with pore metastability with a nucleation barrier at intermediate values of ξ. [40, 42, 43] Conversely, Figure 3a shows that all PMFs computed for the CG systems monotonically increase up to ξ = 1.0. The decrease in slope of the PMF for ξ > 0.6 suggests that peptides lining the pore (Figure 2) help to alleviate the energetic penalty of pore formation; however, there is no nucleation barrier that would indicate possible metastability for larger pore sizes. This behavior and significant overestimates of pore free energies have been observed in the literature before[33, 73] and may be a consequence of higher line tensions and bending moduli of membranes in CG systems. For instance, previous molecular dynamics studies have related the change in the surface tension of POPC membranes with respect to the change in bilayer area through the calculation of the compressibility modulus (K_A) and found that the MARTINI 2.2 force field overestimates K_A by over 100 mN/m compared to the CHARMM36 force field (297 vs. 188 mN/m) using the same run conditions and bilayer size.[74] We also calculated K_A from additional 500 ns simulations of pure DMPC membranes at 323 K and found that MARTINI overestimates K_A by 38% compared to CHARMM (Figure S16), which we interpret as partially responsible for the higher free energy for pore formation in CG (Figure 3a) vs. AA (Figure 3c) simulations at 323 K.

Although ξ has not been tested for AMP-aided pore formation in the literature, similar monotonically increasing PMF trends have been observed in MARTINI systems for the tanh CV[37] applied to DPPC bilayers in the presence of cyclic nonarginines[38] and an adaptation of ξ to combine bilayer fusion and pore formation.[59] Nonetheless, the lower value of ξ at which the PMF slope starts to decrease for MEL (ξ =0.65) compared to MAG and AUR (ξ > 0.7) and the overall larger decrease in PMF relative to the Pure DMPC system (on the order of 40 to 50 kJ/mol) hints at the greater propensity for MEL to form and stabilize pores. The rank-ordering of the PMFs at ξ = 1.0 for the 3 peptide systems also supports observations of equilibrated pore lining (Figure 2). The disordered pore lining of AUR and MAG leads to PMF values between those of the pure DMPC system and MEL system, the latter of which displayed significant toroidal-type pore lining at the upper limit of ξ (Figure 2b). These observations suggest that MARTINI can capture trends in the degree to which peptide pore lining promotes pore formation by reducing corresponding pore nucleation free energies, although the model does not predict metastable, long-lived pores.

Peptides Reduce Pore Nucleation Free Energy Barriers in AA Simulations

To better resolve energetic barriers for pore formation and more accurately capture system interactions, umbrella sampling was performed for AA systems after backmapping final configurations from the 500 ns equilibrated CG configurations. Figure 3b-c shows average PMFs obtained from 3 replicate simulations at both 300 K and 323 K. Standard errors across the 3 replicates are visualized as shaded regions. Consistent with the initial implementation of ξ,[40] the observation of a nucleation barrier (i.e., a PMF maximum) depends upon temperature. There is a clear PMF maximum between ξ = 0.7 and ξ = 0.9 at 300 K (Figure 3b) for all systems, but this barrier is less clear or non-existent depending on the system at 323 K (Figure 3c). Additionally, there is roughly a 10 kJ/mol difference between the 300 K and 323 K systems as expected. Small differences in the values of the energy barrier obtained in this study compared to values reported by Hub et al. for a 128 lipid DMPC bilayer (45.3 vs. ~42 kJ/mol for 300 K and 58.1 vs ~52 kJ/mol for 323 K) using the same CHARMM36 force field can be attributed to the larger 288 lipid DMPC systems used in this study, which has been shown to slightly affect barrier magnitudes.[40]

The key takeaways from the AA PMFs are: (1) all systems exhibit a free energy barrier for pore nucleation, since the PMF always has a positive maximum relative to a flat membrane state (ξ = 0.2) for the conditions studied; (2) there is a local minimum in the PMF at ξ = 1.0 (unlike in CG systems, Figure 3a), which implies the formation of a long-lived metastable pore; (3) the barrier for forming this metastable pore decreases in the presence of peptides (AUR, MEL, MAG) compared to pure DMPC, implying a higher likelihood of pore formation; and (4) AA PMFs show a similar rank ordering of the 4 system types compared to CG PMFs (Figure 3a). We note that expanding the pore to larger sizes not accessible to ξ may decrease the free energy further towards a metastable minimum, which has been demonstrated in a recent extension to the nucleation CV that promotes pore expansion, although we expect the relative values of the barriers to be unchanged.[75] Therefore, the PMF values at $\xi = 1.0$ for the systems in this study are not necessarily metastable free energy minima. Similarly, the difference in free energy between the value of the PMF at $\xi = 1.0$ and the PMF maximum may not correspond to the free energy barrier for pore closing; such a barrier would be higher if the free energy decreases upon pore expansion. For instance, the difference between the free energy of the fully nucleated pore ($\xi = 1.0$) and the PMF maximum for MEL is seemingly low for the AA system at 300 K (Fig. 3b), suggesting rapid pore closing. However, experimental studies have shown that MEL strongly stabilizes long-lived DMPC pores[76], even with a peptide to lipid ratio as low as 1/100 above the critical transition temperature (~=24 °C), indicating that MEL-lined pores do not close rapidly.[77] To confirm that the fully nucleated pore does not close rapidly in simulations, we conducted a 500 ns unbiased simulation starting from the last configuration of the $\xi = 1.0$ window for the AA MEL system at 300 K. Figure S17 shows that the pore not only remains stable but also grows in size during this simulation (Figure S17b), which suggests that the MEL-lined pore may expand after full nucleation past the upper limit of ξ to a more stable, larger pore. These considerations highlight that the PMFs primarily permit analysis of nucleation free energy barriers and the structures of fully nucleated pores.

Of the three peptides, MEL reduces the nucleation free energy barrier to the greatest extent regardless of temperature, with the nucleation barrier decreasing by 35% from 45.3 kJ/mol to 29.3 kJ/mol at 300 K and by 44% from 58.1 kJ/mol to 32.2 kJ/mol. This decrease is consistent with the ability of MEL to act as a pore-forming AMP, and is comparable to similar decreases in nucleation free energy barriers predicted for POPC membranes in the presence of other pore-forming compounds, such as the antifungal drug itraconazole[42] and polycationic species.[43] At 300 K, both AUR and MAG have similar free energy barriers for pore nucleation (~38-40 kJ/mol); however, the PMF at $\xi = 1.0$ is significantly decreased for MAG compared to AUR. These results suggest that while barriers to pore formation are similar for both peptides, the increased energetic stability of MAG-lined pores for larges values of ξ (corresponding to fully nucleated pores) would lead to longer-lived pores once formed, especially given the sharp decrease in the PMF slope past the nucleation barrier for MAG compared to AUR and MEL (Figure 3b). However, as noted above, confirming this increase in pore stability would require further analysis of larger pore sizes. Nonetheless, these results are consistent with experimental observations that MEL promotes pore formation, AUR does not, and MAG exhibits behavior between these extremes.

Melittin Pore Structure Differs from Other Peptide-Containing Systems

We next sought to understand differences in the PMFs by analyzing the simulation configurations at full pore nucleation ($\xi = 1.0$) and relating simulation observations to known mechanisms of pore formation. We first performed number density analysis for each system at 300 K to study the spatial distribution of different system components. Starting from the radial and z center of the pore, atomic positions obtained from the last 20 ns of each trajectory were histogrammed into bins with radius 0.1 nm (from 0 to 5 nm) and height 0.1 nm in z direction (from -3.5 to 3.5 nm), and the number of atoms for each group present per bin was divided by bin volume in nm^3 using an in-house python script.

Figure 4 shows number densities for the phosphates of DMPC and oxygen atoms of water (biased as part of ξ), all peptide atoms, and Cl- counterions, with horizontal lines indicating the approximate regions corresponding to DMPC head groups. Using the pure DMPC system (Figure 4a) as reference, there is a clear correlation between the densities of DMPC head phosphate groups and water oxygen atoms when a pore with a maximum diameter of roughly 2 nm is formed at ξ=1.0, which is because lipid head groups deform to line the pore and alleviate unfavorable water-lipid tail interactions. This pore size during full nucleation and hourglass shape is consistent with previous studies of pores that have conducted group density analysis with the implementation of this CV.[42, 78, 79]

Comparing DMPC head phosphate and water oxygen profiles with peptide-containing systems (Figure 4 b-d), the 8 AUR system (Figure 4b) only alleviates pore phosphate density slightly, and the peptide density indicates that there is tight clustering amongst the peptides but no full pore lining between upper and lower leaflets. This peptide clustering behavior is consistent with equilibrated CG systems at the ξ=1.0 sampling window (Figure 2a). Conversely, the 8 MEL system (Figure 4c) shows a significant decrease in head phosphate density across the length of the pore and near 0 nm^{-3} density within the middle 0.5 nm. This is supported by the large peptide number density across the full range of the membrane. Interestingly, the elliptical character of the nucleated pore is also diminished as the pore appears to reach a size of close to 3 nm. This more squarish water profile could be indicative of a higher likelihood of a structured toroidal pore mechanism of MEL relative to AUR and MAG peptides (further supported with visualizations of pore structures across replicate trials in Figure S4), similar to previous findings in the literature for both experimental[19, 77] and computational[29] studies. Additionally, the 8 MEL system is the only system with a substantial counterion density in the pore, implying the formation of a larger, more permissive pore.

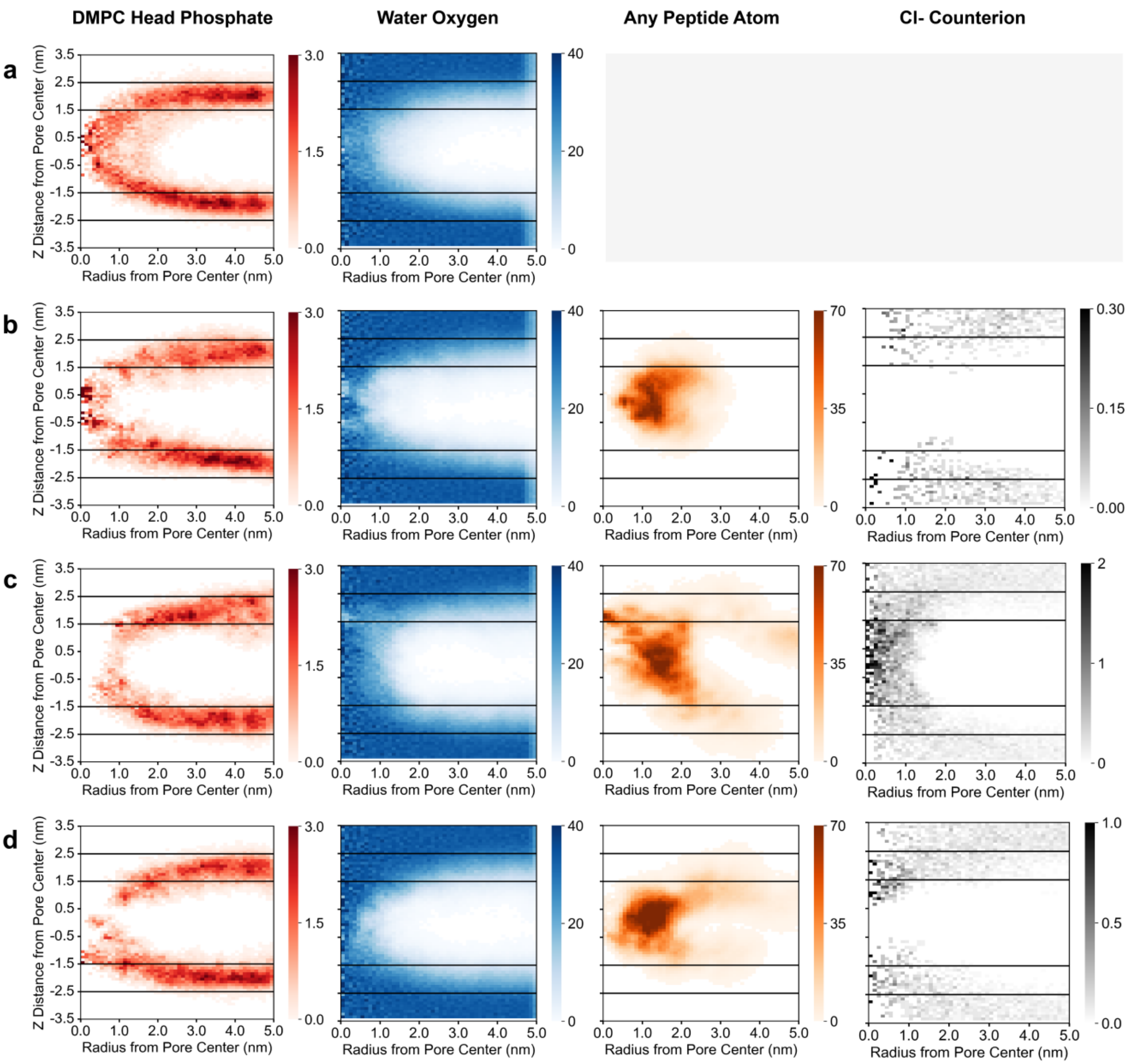

Figure 4: Group number densities (nm^{-3}) from AA umbrella sampling trajectories for $\xi = 1.0$. Number densities are shown for DMPC lipid head phosphate groups, water oxygen atoms, any peptide atom, and Cl- counterions for (a) Pure DMPC, (b) 8 AUR, (c) 8 MEL, and (d) 8 MAG. Number density heat maps are based on 0.1 nm bins for the distance projected onto the *z*-axis (*z*-distance) and radial distance in the *xy*-plane away from the geometric center of the pore in the membrane. Horizontal black lines on each plot represent the fluctuation range of DMPC head phosphates. All replicate and trial-averaged number density profiles are provided in Figures S23-S24.

The 8 MAG system (Figure 4d) demonstrates some decrease in phosphate density near the upper but not lower membrane leaflet, and the peptide density confirms that MAG prefers to remain near the upper leaflet after membrane binding compared to MEL. Further analysis of the AA umbrella sampling trajectories (described below) details this observation; however, one simple explanation is that pores of ~2 nm diameter are not large enough to adequately incorporate all 8 peptides given prior literature that MAG-induced pores of up to 8 nm in diameter have been resolved in lipid vesicles using neutron scattering and cryo-EM.[72] However, MAG pore diameters of 2-4 nm have also been resolved using fluorescence and neutron-scattering studies.[80, 81] Taken together, these results point to MAG preferring larger pore sizes than the upper limit of ξ, which supports free energy trends discussed for this peptide (Figure 3b).

Peptide Tilt Angles Corroborate Melittin's Increased Propensity to Line Pores

To better quantify the pore-lining propensity of each peptide, peptide tilt angles were calculated from the umbrella sampling production trajectories at different stages of the pore nucleation process. The tilt angle of each peptide was defined as the average angle between the vector connecting the N-terminus backbone nitrogen to the C-terminus backbone carbon and the membrane *xy*-plane. Angles close to 0° indicate peptides lying approximately in the plane of the membrane that are adsorbed to the membrane surface whereas angles close to 90° indicate peptides aligned parallel to the membrane normal that are lining the pore. Figure 5a shows time-averaged peptide tilt angles with highlighted regions indicating ranges of tilt angles for membrane-bound peptides in the absence of the pore ($\xi = 0.2$). Figures 5b-5d show representative system configurations at the onset of peptide pore lining ($\xi = 0.7$ or 0.8) and for fully nucleated pores ($\xi = 1.0$) for all three peptides. Similar trends are observed for all three replicas as shown in Figure S18.

The tilt angles in Figure 5a indicate that MEL is capable of lining aqueous pores at earlier stages in the nucleation process ($\xi = 0.7$) relative to AUR and MAG ($\xi = 0.8$) as indicated by values much larger than the tilt-angles in the pore-free membranes. Simulation snapshots (Figure 5c) and the large tilt angles indicate that 3 MEL peptides line the pore for $\xi = 0.7$ with the tight tilt angle distribution suggesting the formation of well-ordered toroidal-type pores. This result is consistent with previous MD simulations in DPPC bilayers that have shown that the N-terminus of MEL has a strong affinity for small local defects in membranes induced by thermal fluctuations, where the insertion of 1 MEL leads to a cooperative response of other MEL inserting their N-termini into the defect[68, 82]. This behavior can be largely attributed to the affinity of the largely hydrophobic N-terminus of MEL to the lipid tail region of membranes[83]. In comparison, only 1 peptide begins to line the pore starting at $\xi = 0.8$ for AUR (Figure 5b) and MAG (Figure 5d). These results are consistent with the CG (Figure 3a) and AA (Figure 3b-c) free energy profiles, in which MEL introduces either a kink in the PMF or a decrease in the PMF at a smaller value of ξ than the other two peptides, pointing to the effect of peptide-stabilized pores on these PMFs. Additionally, at full nucleation ($\xi = 1.0$), there is some peptide diffusion to the lower leaflet for AUR and MAG but not for MEL as shown in Figure 5. The absence of MEL diffusion can be attributed to the strong anchoring of the highly cationic C-terminus of MEL to the lipid phosphate region of the upper leaflet, which has been corroborated by previous computational studies.[68, 84]

At full nucleation ($\xi = 1.0$), only 2 MAG peptides have lined the pore in a transmembrane orientation (based on large tilt angles) compared to 5 and 6 for AUR and MEL respectively, suggesting that MAG less efficiently stabilizes membrane pores. The snapshots indicate that most MAG peptides instead retain a more disordered structure and stay in membrane-bound states near the pore. For AUR and MEL, the wider range of tilt angles (~30 degrees for AUR compared to ~20 degrees for MEL) at $\xi = 1.0$ suggests a more disordered pore structure (Figure 5a) despite a similar number of peptides lining the pore. This disordered behavior for AUR is similar to a previous MD study in which 5 AUR peptides were pre-configured to vertically line a DPPC pore at similar peptide to lipid ratios as our study (1:25 vs. 1:36 for our systems), with large tilt angle ranges of 15-80 degrees.[85] The consistent observation of disordered structures in both studies indicates that AUR is unlikely to form structured toroidal pores even in simple short-tail (DMPC and DPPC) lipid bilayers, which agrees with the less favorable free energy of pore formation observed in the PMFs. Together, these results support the general variations in the PMFs for the three peptides (Figure 3b) and indicate that the PMF for MEL has the earliest decrease in slope and lowest energetic barrier for nucleation across the 4 systems studied due to its stronger propensity to line pores in ordered structures.

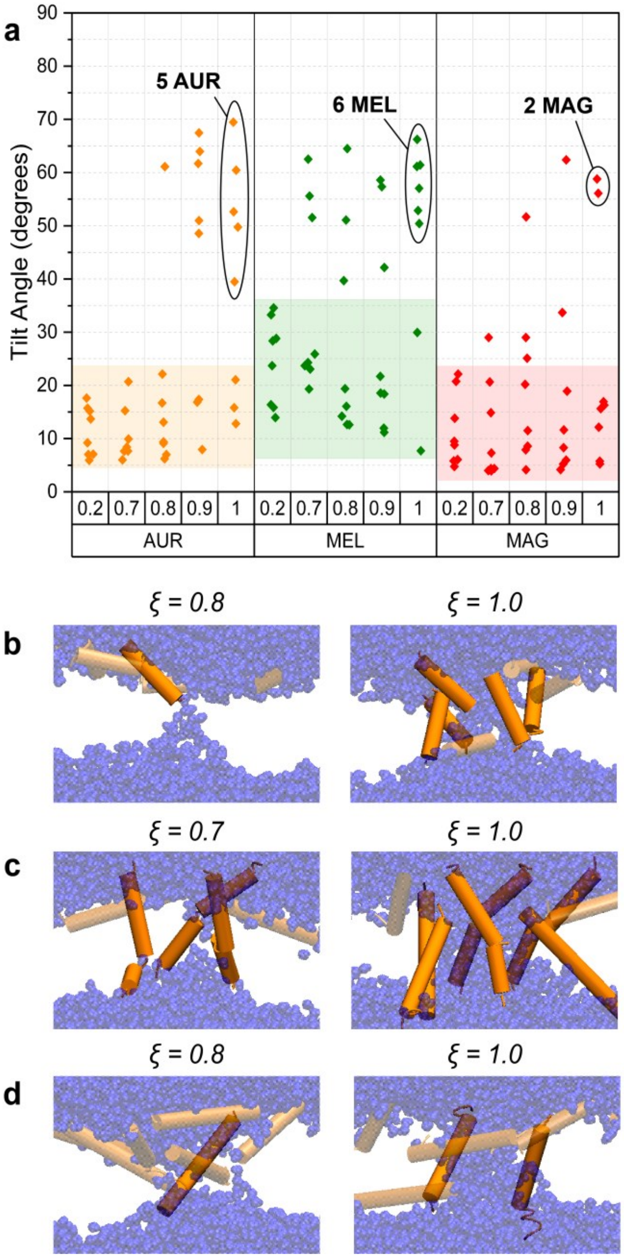

Figure 5: (a) Tilt angles vs. ξ for each of the 8 peptides in the Aurein 1.2 (AUR), Melittin (MEL), and Magainin 2 (MAG) AA systems at 300 K. Shaded regions indicate the range of tilt angles for the pore-free membrane at ξ = 0.2. (b-d) Simulation configurations at the onset and end of pore formation for the (b) AUR, (c) MEL, and (d) MAG systems. All peptides are represented as orange cylinders; opaque peptides are lining the pore and semi-transparent peptides are not. Water molecules are represented as transparent blue spheres.

Pore Formation Alleviates Lipid Disruption Associated with Peptide Binding

Based on the relatively ordered structures observed for MEL-lined pores (Figures 4 and 5) compared to the other peptides, we next sought to determine if the disruption of lipid structure due to peptide interactions and pore formation could be related to the PMF trends. A common metric for quantifying lipid structural order is the deuterium order parameter (S_{CD}), which measures the alignment of lipid tail bonds (θ) relative to the membrane normal and is defined in Equation 3:

$$S_{CD} = < \frac{3}{2}\cos^2\theta - \frac{1}{2} > \tag{3}$$

Larger values (up to 1) indicate a higher degree of alignment of lipid tails to the membrane normal. This parameter has been extensively utilized in the literature to quantify lipid order in membrane simulations[86], including due to changes in the value of ξ.[43, 79] We calculated S_{CD} relative to the DMPC membrane normal (taken as the *z*-axis of the simulation box). Figure 6a shows variation in S_{CD} for the pore-free membrane (ξ = 0.2) and fully nucleated pore (ξ = 1.0) for one tail of the DMPC lipids; values for the other tail exhibit similar trends and are shown in Figure S19. Additionally, to compare lipid order profiles for lipids within close proximity of the fully nucleated pore (ξ = 1.0), Figure 6c shows values of S_{CD} for lipids with head phosphate groups that are within a 2 nm radial distance of the pore center (schematically illustrated in Figure 6b), which we refer to as radial S_{CD} values.

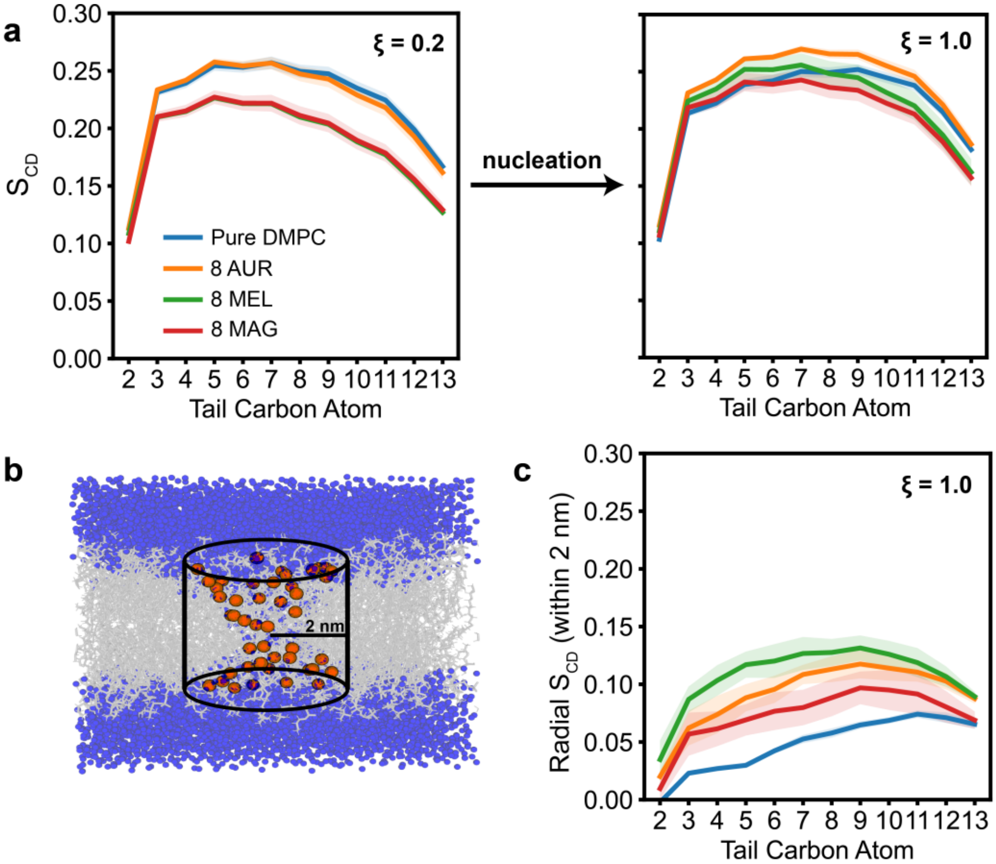

Figure 6: Deuterium order parameter (S_{CD}) values for atoms in one tail of DMPC for AA systems at 300 K. Values for the other tail are shown in Figure S19. (a) S_{CD} for a pore-free membrane (ξ = 0.2) and fully nucleated pore (ξ = 1.0). (b) Schematic showing the lipid groups used to compute radial S_{CD} values, which include DMPC lipids with head phosphates (orange spheres) within a 2 nm radial distance (in the *xy*-plane) of the pore center. (c) Radial S_{CD} values for the fully nucleated pore (ξ = 1.0). Error bars indicate the standard error computed from three replicates (Figures S20-S22).

For $\xi = 0.2$, the binding of 8 MEL (green) or 8 MAG (red) peptides to the membrane disrupt lipid tail structure relative to the Pure DMPC case (blue), which is apparent from the decrease in S_{CD} values. By comparison, 8 AUR peptides (orange) have a minimal effect on lipid order when bound to the membrane. The difference between these peptides can be attributed to the higher positive charge density of MEL and MAG peptides compared to AUR and generally agree with prior results indicating membrane disruption upon MEL and MAG binding. For example, previous studies of MEL interactions with POPC-POPG bilayers have observed conformational realignments of lipids given the large influx of positive surface charge upon peptide binding, leading to orientation changes in the choline head group.[87] For MAG, reductions in lipid tail order parameters of up to 25% have been observed for a variety of membrane types when 2 mol% peptide (roughly 1:50 P/L ratio) are bound based upon quadrupolar splittings of the ^{2}H-NMR spectra.[88] Additionally, experimental measurements have shown that increasing MAG adsorption leads to decreases in bilayer thickness in DMPC[89], which would also lead to increased tail disorder at $\xi = 0.2$.

Once the pore is fully nucleated ($\xi = 1.0$ in Figure 6b), the S_{CD} values for the pure DMPC system decrease as expected compared to $\xi = 0.2$ due to lipids bending towards the hydrophilic pore; such disruption is energetically unfavorable. For the AUR system, S_{CD} values remain similar for both $\xi = 0.2$ and $\xi = 1.0$, with values in the latter case again similar to the S_{CD} values for the pore-free pure DMPC membrane. This comparison indicates that the 5 AUR peptides lining the pore alleviate tail disruption and thus decrease the energy for pore formation, which can explain the decrease in the PMF at $\xi = 1.0$ for the AUR system compared to pure DMPC (Figure 3b). For both the MEL and MAG systems, S_{CD} values increase for $\xi = 1.0$ to obtain values similar to those of pure DMPC in the pore-free membrane ($\xi = 0.2$). Counterintuitively, this result indicates that the disruption of lipid order due to binding of these peptides to the membrane in the absence of the pore is alleviated upon pore formation, which we attribute to the motion of peptides from membrane-bound regions to pore-lining structures. This favorable change in S_{CD} values is in agreement with the PMFs for these peptides, which show deeper minima at $\xi = 1.0$ than the AUR peptides (Figure 3b), and which we can attribute to the decreased penalty for lipid disruption upon pore nucleation.

To further support this hypothesis that lipid bending during pore formation is partially alleviated by peptide lining of the pore, Figure 6c presents radial S_{CD} values to highlight lipid tail disruption for those lipids close to the pore itself. These values again support trends in the PMFs observed for the 4 systems (Figure 3b) – all peptides lead to lipid order parameters more similar (larger) to the pore-free system (pure DMPC in Figure 6a) indicating that peptide pore lining reduces the need for lipids to deform such that that phosphate head groups line the pore. MEL has the largest radial S_{CD} values of the peptide-containing systems, pointing to its increased propensity to reduce lipid deformation and supporting the data in Figures 4 and 5.

Pore Lining by Magainin 2 is Influenced by Salt Bridge Formation

The analysis in Figures 4-6 supports the ability of MEL to most effectively stabilize pore formation through pore lining, while AUR least effectively does so, explaining the difference between these peptides in the PMFs shown in Figure 3b. The lipid tail order data also supports why MAG can have a metastable PMF minimum comparable to MEL by alleviating lipid disruption to a similar extent. The PMF barrier for MAG at $\xi = 0.8$, however, is large and comparable to AUR, which merits further analysis. Motivated by the low Cl- number densities observed for AUR and MAG within the pore center (Figure 4b and d) and the presence of both positively and negatively charged sidechains compared to MEL (Figure 1a and c), we next sought to calculate the propensity for AUR and MAG peptides to form salt bridges as a function of ξ to determine if these strong peptide-peptide interactions affect trends in the PMFs. Previous studies have suggested that salt bridges between peptides stabilize their alpha-helical secondary structure[90-92] and can lead to stabilized heterodimers in membranes that precede pore formation.[93]

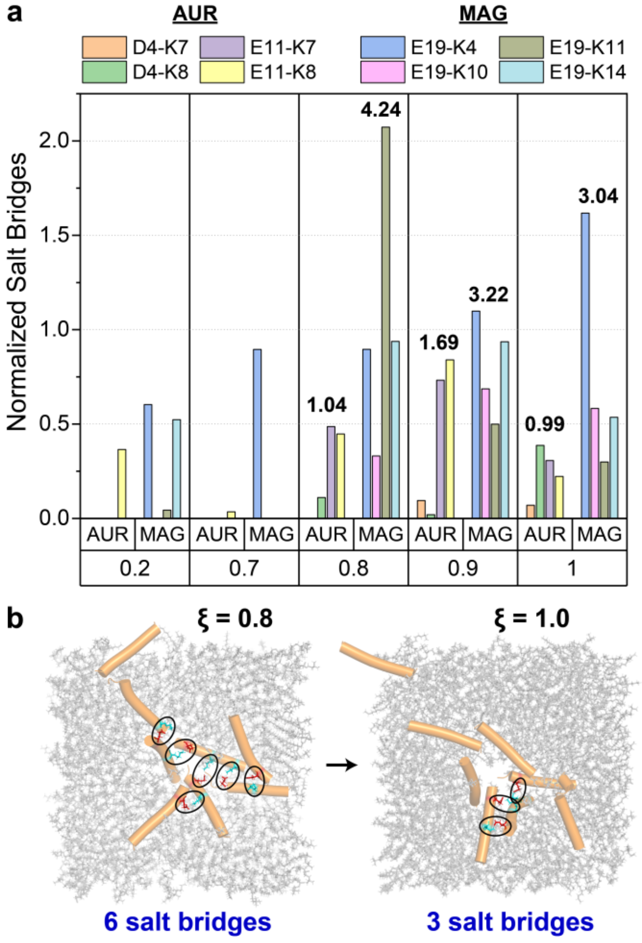

Figure 7: Comparison of salt bridge formation between Aurein 1.2 (AUR) and Magainin 2 (MAG) peptides at representative ξ values for the pore-free membrane (ξ = 0.2) compared to pore formation (ξ = 0.7, 0.8, 0.9, 1.0) AA system at 300 K. (a) Normalized salt bridge values for AUR and MAG. Bold numbers indicate the sum across all four salt bridge types. (b) Top-down simulation view of salt bridges formed for MAG at ξ = 0.8 (beginning of peptide pore lining) vs. ξ = 1.0 (fully nucleated pore). Peptides are shown as orange cylinders, negative E sidechains as red sticks, positive K sidechains as cyan sticks, and DMPC lipids as grey sticks. Salt bridges are circled.

AUR peptides have 2 cationic (K7, K8) and 2 anionic side chains (D4, E11), whereas MAG peptides have 4 cationic (K4, K10, K11, K14) and 1 anionic (E19) side chain, so there are 4 possible types of salt bridge to consider for each peptide. We calculated the number of salt bridges for different values of ξ by defining a salt bridge as consisting of a nitrogen atom of a basic residue (K) and oxygen atom of an acid residue (D, E) within 0.4 nm of each other. We further defined the number of 'normalized salt bridges' as the total number of configurations in which a particular type of salt bridge (among the four possible) was observed in each umbrella sampling window divided by the total number of configurations (Figure S25).

Figure 7a compares the number of normalized salt bridges (averaged across three replicates) for AUR and MAG peptides at four different values of ξ. For both peptides, there is negligible salt bridge formation for ξ values prior to pore formation and peptide lining of the pore ($\xi = 0.2, 0.7$). Interestingly, at the beginning of pore lining for both peptides ($\xi = 0.8$), MAG has over 4 times the probability to form salt bridges relative to AUR across all types of salt bridges. To understand this behavior for MAG, we analyzed all salt bridges sustained for at least half of the timesteps in the $\xi = 0.8$ umbrella sampling window (defined as 'long-lasting salt bridges') and identified 6 long-lasting salt bridges in the first simulation replica (visualized in Figure 7b, $\xi = 0.8$). By comparison, salt bridges for AUR were more transient in nature, with only 1 long-lasting salt bridge during any of the three replicate simulations.

This chain of salt bridges across the pore opening for the 8 MAG system and the much higher propensity for salt bridge formation in general over AUR could lead to the sharp peak in the PMF for this system prior to the $\xi = 0.8$ window (Figure 3b), which is not seen in any other system studied. This is further supported by the decrease in overall salt bridges for MAG as the pore becomes larger ($\xi = 0.9, 1.0$). In the visualization of the $\xi = 1.0$ window (Figure 7b), there appears to be a restructuring of salt bridges to stabilize one of the two MAG peptides lining the fully nucleated pore (Figure 5a and d). With these results, we hypothesize the following behavior during pore formation in the 8 MAG system: (1) salt bridges force MAG peptides into unfavorable "disordered" pore lining configurations at the early stages of nucleation ($0.7 < \xi < 0.8$), leading to the sharp, large peak in the PMF for pore formation; (2) increasing the pore size ($\xi > 0.8$) releases spatial constraints on MAG and permits the peptides to span the pore and interact with counterions, leading to a significant decrease in the nucleation free energy (Figure 3b). These behaviors would be unique to MAG due to its strong propensity for salt bridge formation among the three peptides studied.

Conclusions

In this study, we have provided a generalizable methodology for investigating the energetics of membrane pore nucleation and pore lining by membrane-active species. Through the implementation of a hysteresis-free nucleation collective variable (ξ)[40], we have shown that a CG-to-AA backmapping approach can be utilized to first equilibrate peptide positions quickly around a nucleating pore with MARTINI CG representations of lipids and peptides before then backmapping these systems to the CHARMM36 AA force field to resolve free energy profiles for pore formation in atomistic detail. The key advantage of this methodology over previous studies is that pore formation in membranes can be observed as a result of natural peptide clustering and lateral diffusion rather than having to bias peptide configurations around a pore *a priori*.

To our knowledge, this has allowed us for the first time to resolve energetic barriers for pore formation for the antimicrobial peptides aurein 1.2, melittin, and magainin 2 from AA MD simulations without direct biases on whole lipids or peptides and without predefining peptide positions relative to the pore. Comparison of pore formation free energies resolved with umbrella sampling for both the CG and AA systems validated the need for the backmapping approach because only the AA simulations demonstrated expected free energy barriers, which is likely due to overestimations of membrane line tensions and bending moduli in the MARTINI force field. Nonetheless, both CG and AA free energy profiles demonstrated Melittin's increased propensity to line pores in DMPC membranes at smaller pore sizes (lower ξ values), and both CG and AA simulations predict lower free energy barriers for pore formation for melittin compared to aurein 1.2 and magainin 2. These calculations are in good agreement with literature findings that melittin promotes pore formation as a mechanism of antimicrobial activity.[19, 20, 25, 77, 94]

To understand the peptide-mediated differences in pore formation free energies, we analyzed the AA simulation trajectories to quantify peptide, pore, and lipid structure through calculation of densities, peptide tilt angles, the deuterium order parameter (S_{CD}), and intermolecular peptide salt bridges. Our main conclusions are as follows: (1) Aurein 1.2 lines pores in a disordered structure and does little to alleviate either DMPC head phosphate density in the pore or lipid deformations in general upon pore lining, leading to the smallest decrease in the pore nucleation free energy barrier; (2) Melittin is the best pore former of the peptides studied as supported by strong toroidal-type behavior in tilt angle and group density analysis as well as clear alleviation of lipid deformation adjacent to the pore, leading to the largest decrease in the pore nucleation free energy barrier; (3) Magainin 2 has a weak propensity to line pores with only ~2-3 peptides lining the pore at the maximum value of ξ, which appears to be due to salt bridges between peptides and leads to a large pore nucleation free energy barrier. However, magainin 2 also introduces lipid disruption upon membrane binding that is alleviated when a pore forms, leading to a comparable decrease in the free energy of the nucleated pore (ξ=1.0) as melittin.

We note that even in the presence of pore-lining peptides the pore nucleation barriers predicted by the AA simulations are large compared to thermal energy (*e.g.*, the pore nucleation barrier for melittin in Fig. 3b is 11.8 k_BT, where k_B is Boltzmann's constant and T is temperature), suggesting that pore formation should be rare. However, a limitation of our study is that peptide concentration effects are not evaluated given the fixed 1/36 peptide to lipid ratio (P/L) for all systems. Experimental studies have shown that increasing peptide concentration in lipid membranes leads to increased area per lipid and lateral tension which are precursors to pore formation once a critical peptide concentration is reached.[95, 96] For example, pore formation by magainin 2 has been proposed to be 'stretch-activated' based on experiments finding that the fractional change in area of DOPC:PG GUVs is directly proportional to the surface concentration of MAG and pore formation rate constants are greatly increased with increasing GUV area.[71, 97] For melittin, peptide flip-flop to the inner leaflet of DOPC:PG GUVs has been observed to occur prior to pore formation with a proposed critical P/L of 1/45[19]; however, spontaneous pore formation in MARTINI simulations of DPPC bilayers has only been observed within 2 µs at very large P/L (~1/21) with half of the peptides initiated in the lower leaflet.[25] Therefore, further analysis on differing P/L for melittin and magainin 2 using the methodology is this work could provide a better understanding of the concentration-dependent effects of these peptides on the free energy barrier, along with a systematic exploration of membrane tension effects at differing P/L. Similarly, future work will also consider whether increasing the pore size, such as through implementation of the expansion CV proposed recently[75], leads to increased pore lining by magainin 2 and further stabilization of pore formation in the CG and AA simulations. Overall, the results of our study illustrate the atomistic insights achievable from the combined CG and AA simulation approach, which we believe will provide a framework for future efforts to quantify clinically applicable activity and pore formation metrics for varied antimicrobial materials.

Description of Supporting Information

The supporting information includes a single PDF file with 25 figures and additional information on the computational workflow, simulation setup and parameters, PMF convergence analysis, and replicate simulation trials and analysis to support results and figures in the manuscript. The supporting information also includes a .zip file containing all PLUMED files used to implement the collective variable in this work, along with documentation. Raw simulation data, scripts to run the simulations and trajectory analysis, Gromacs/PLUMED files, and analysis scripts and data have been uploaded to a Dryad repository associated with this manuscript (https://doi.org/10.5061/dryad.vq83bk42v) to facilitate reproducibility of the results in this work.

Acknowledgements

This material is based upon work supported by the National Science Foundation under award DMR-2044997. This work used the Advanced Cyberinfrastructure Coordination Ecosystem: Services & Support (ACCESS), which is supported by the National Science Foundation under Grant No. 2138307. J.D.R. and R.C.V.L. also thank Carlos A. Huang-Zhu for assistance with development of some of the analysis tools used in this manuscript.

References

(1) Akram, F.; Imtiaz, M.; Haq, I. u. Emergent crisis of antibiotic resistance: A silent pandemic threat to 21st century. *Microbial Pathogenesis* **2023**, *174*, 105923. DOI: https://doi.org/10.1016/j.micpath.2022.105923.

(2) Srinivasan, R.; Santhakumari, S.; Poonguzhali, P.; Geetha, M.; Dyavaiah, M.; Xiangmin, L. Bacterial Biofilm Inhibition: A Focused Review on Recent Therapeutic Strategies for Combating the Biofilm Mediated Infections. *Frontiers in Microbiology* **2021**, *12*, 676458.

(3) Hall-Stoodley, L.; Costerton, J. W.; Stoodley, P. Bacterial biofilms: from the Natural environment to infectious diseases. *Nature Reviews Microbiology* **2004**, *2* (2), 95-108. DOI: 10.1038/nrmicro821.

(4) El-Khoury, C.; Mansour, E.; Yuliandra, Y.; Lai, F.; Hawkins, B. A.; Du, J. J.; Sundberg, E. J.; Sluis-Cremer, N.; Hibbs, D. E.; Groundwater, P. W. The role of adjuvants in overcoming antibacterial resistance due to enzymatic drug modification. *RSC Medicinal Chemistry* **2022**, *13* (11), 1276-1299, 10.1039/D2MD00263A. DOI: 10.1039/D2MD00263A.

(5) Du, D.; Wang-Kan, X.; Neuberger, A.; van Veen, H. W.; Pos, K. M.; Piddock, L. J. V.; Luisi, B. F. Multidrug efflux pumps: structure, function and regulation. *Nature Reviews Microbiology* **2018**, *16* (9), 523-539. DOI: 10.1038/s41579-018-0048-6.

(6) Benfield, A. H.; Henriques, S. T. Mode-of-Action of Antimicrobial Peptides: Membrane Disruption vs. Intracellular Mechanisms. *Frontiers in Medical Technology* **2020**, *2*, 610997.

(7) Hanson, M. A.; Dostálová, A.; Ceroni, C.; Poidevin, M.; Kondo, S.; Lemaitre, B. Synergy and remarkable specificity of antimicrobial peptides in vivo using a systematic knockout approach. *eLife* **2019**, *8*, e44341. DOI: 10.7554/eLife.44341.

(8) Lei, J.; Sun, L.; Huang, S.; Zhu, C.; Li, P.; He, J.; Mackey, V.; Coy, D. H.; He, Q. The antimicrobial peptides and their potential clinical applications. *Am J Transl Res* **2019**, *11* (7), 3919-3931.

(9) Starr, C. G.; Wimley, W. C. Antimicrobial peptides are degraded by the cytosolic proteases of human erythrocytes. *Biochimica et Biophysica Acta (BBA) - Biomembranes* **2017**, *1859* (12), 2319-2326. DOI: https://doi.org/10.1016/j.bbamem.2017.09.008.

(10) Lu, J.; Xu, H.; Xia, J.; Ma, J.; Xu, J.; Li, Y.; Feng, J. D- and Unnatural Amino Acid Substituted Antimicrobial Peptides With Improved Proteolytic Resistance and Their Proteolytic Degradation Characteristics. *Frontiers in Microbiology* **2020**, *11*, 563030.

(11) Lee, M.-R.; Raman, N.; Gellman, S. H.; Lynn, D. M.; Palecek, S. P. Incorporation of β-Amino Acids Enhances the Antifungal Activity and Selectivity of the Helical Antimicrobial Peptide Aurein 1.2. *ACS Chemical Biology* **2017**, *12* (12), 2975-2980. DOI: 10.1021/acschembio.7b00843.

(12) Li, J.; Koh, J.-J.; Liu, S.; Lakshminarayanan, R.; Verma, C. S.; Beuerman, R. W. Membrane Active Antimicrobial Peptides: Translating Mechanistic Insights to Design. *Frontiers in Neuroscience* **2017**, *11*, 73.

(13) Mudhakir, D.; Harashima, H. Learning from the Viral Journey: How to Enter Cells and How to Overcome Intracellular Barriers to Reach the Nucleus. *The AAPS journal* **2009**, *11*, 65-77. DOI: 10.1208/s12248-009-9080-9.

(14) Shai, Y.; Oren, Z. From "carpet" mechanism to de-novo designed diastereomeric cell-selective antimicrobial peptides. *Peptides* **2001**, *22* (10), 1629-1641. DOI: https://doi.org/10.1016/S0196-9781(01)00498-3.

(15) Shahmiri, M.; Enciso, M.; Mechler, A. Controls and constrains of the membrane disrupting action of Aurein 1.2. *Scientific Reports* **2015**, *5* (1), 16378. DOI: 10.1038/srep16378.

(16) Fernandez, D. I.; Le Brun, A. P.; Whitwell, T. C.; Sani, M.-A.; James, M.; Separovic, F. The antimicrobial peptide aurein 1.2 disrupts model membranes via the carpet mechanism. *Physical Chemistry Chemical Physics* **2012**, *14* (45), 15739-15751, 10.1039/C2CP43099A. DOI: 10.1039/C2CP43099A.

(17) Liao, F.; Chen, Y.; Shu, A.; Chen, X.; Wang, T.; Jiang, Y.; Ma, C.; Zhou, M.; Chen, T.; Shaw, C.; et al. A Novel Strategy for the Design of Aurein 1.2 Analogs with Enhanced Bioactivities by Conjunction of Cell-Penetrating Regions. *Antibiotics* **2023**, *12* (2), 412. DOI: 10.3390/antibiotics12020412.

(18) Rady, I.; Siddiqui, I. A.; Rady, M.; Mukhtar, H. Melittin, a major peptide component of bee venom, and its conjugates in cancer therapy. *Cancer Lett* **2017**, *402*, 16-31. DOI: 10.1016/j.canlet.2017.05.010.

(19) Lee, M.-T.; Sun, T.-L.; Hung, W.-C.; Huang, H. W. Process of inducing pores in membranes by melittin. *Proceedings of the National Academy of Sciences* **2013**, *110* (35), 14243-14248. DOI: 10.1073/pnas.1307010110.

(20) van den Bogaart, G.; Guzmán, J. V.; Mika, J. T.; Poolman, B. On the mechanism of pore formation by melittin. *J Biol Chem* **2008**, *283* (49), 33854-33857. DOI: 10.1074/jbc.M805171200.

(21) Tuerkova, A.; Kabelka, I.; Králová, T.; Sukeník, L.; Pokorná, Š.; Hof, M.; Vácha, R. Effect of helical kink in antimicrobial peptides on membrane pore formation. *eLife* **2020**, *9*, e47946. DOI: 10.7554/eLife.47946.

(22) Illya, G.; Deserno, M. Coarse-Grained Simulation Studies of Peptide-Induced Pore Formation. *Biophysical Journal* **2008**, *95* (9), 4163-4173. DOI: https://doi.org/10.1529/biophysj.108.131300.

(23) Vácha, R.; Frenkel, D. Simulations Suggest Possible Novel Membrane Pore Structure. *Langmuir* **2014**, *30* (5), 1304-1310. DOI: 10.1021/la402727a.

(24) Kabelka, I.; Vácha, R. Advances in Molecular Understanding of α-Helical Membrane-Active Peptides. *Accounts of Chemical Research* **2021**, *54* (9), 2196-2204. DOI: 10.1021/acs.accounts.1c00047.

(25) Santo, K. P.; Berkowitz, M. L. Difference between Magainin-2 and Melittin Assemblies in Phosphatidylcholine Bilayers: Results from Coarse-Grained Simulations. *The Journal of Physical Chemistry B* **2012**, *116* (9), 3021-3030. DOI: 10.1021/jp212018f.

(26) Sengupta, D.; Leontiadou, H.; Mark, A. E.; Marrink, S.-J. Toroidal pores formed by antimicrobial peptides show significant disorder. *Biochimica et Biophysica Acta (BBA) - Biomembranes* **2008**, *1778* (10), 2308-2317. DOI: https://doi.org/10.1016/j.bbamem.2008.06.007.

(27) Lipkin, R.; Lazaridis, T. Computational studies of peptide-induced membrane pore formation. *Philos Trans R Soc Lond B Biol Sci* **2017**, *372* (1726), 20160219. DOI: 10.1098/rstb.2016.0219.

(28) Miyazaki, Y.; Okazaki, S.; Shinoda, W. Free energy analysis of membrane pore formation process in the presence of multiple melittin peptides. *Biochimica et Biophysica Acta (BBA) - Biomembranes* **2019**, *1861* (7), 1409-1419. DOI: https://doi.org/10.1016/j.bbamem.2019.03.002.

(29) Leveritt, J. M., 3rd; Pino-Angeles, A.; Lazaridis, T. The structure of a melittin-stabilized pore. *Biophys J* **2015**, *108* (10), 2424-2426. DOI: 10.1016/j.bpj.2015.04.006.

(30) Patel, S. J.; Van Lehn, R. C. Characterizing the Molecular Mechanisms for Flipping Charged Peptide Flanking Loops across a Lipid Bilayer. *The Journal of Physical Chemistry B* **2018**, *122* (45), 10337-10348. DOI: 10.1021/acs.jpcb.8b06613.

(31) Herce, H. D.; Garcia, A. E. Molecular dynamics simulations suggest a mechanism for translocation of the HIV-1 TAT peptide across lipid membranes. *Proceedings of the National Academy of Sciences* **2007**, *104* (52), 20805-20810. DOI: 10.1073/pnas.0706574105.

(32) Leontiadou, H.; Mark, A. E.; Marrink, S. J. Molecular dynamics simulations of hydrophilic pores in lipid bilayers. *Biophys J* **2004**, *86* (4), 2156-2164. DOI: 10.1016/s0006-3495(04)74275-7.

(33) Bennett, W. F. D.; Tieleman, D. P. Water Defect and Pore Formation in Atomistic and Coarse-Grained Lipid Membranes: Pushing the Limits of Coarse Graining. *Journal of Chemical Theory and Computation* **2011**, *7* (9), 2981-2988. DOI: 10.1021/ct200291v.

(34) Patel, S. J.; Van Lehn, R. C. Analysis of Charged Peptide Loop-Flipping across a Lipid Bilayer Using the String Method with Swarms of Trajectories. *The Journal of Physical Chemistry B* **2021**, *125* (22), 5862-5873. DOI: 10.1021/acs.jpcb.1c02810.

(35) You, W.; Tang, Z.; Chang, C.-e. A. Potential Mean Force from Umbrella Sampling Simulations: What Can We Learn and What Is Missed? *Journal of Chemical Theory and Computation* **2019**, *15* (4), 2433-2443. DOI: 10.1021/acs.jctc.8b01142.

(36) Kumar, S.; Rosenberg, J. M.; Bouzida, D.; Swendsen, R. H.; Kollman, P. A. THE weighted histogram analysis method for free-energy calculations on biomolecules. I. The method. *Journal of Computational Chemistry* **1992**, *13* (8), 1011-1021. DOI: https://doi.org/10.1002/jcc.540130812.

(37) Tolpekina, T. V.; den Otter, W. K.; Briels, W. J. Nucleation free energy of pore formation in an amphiphilic bilayer studied by molecular dynamics simulations. *The Journal of Chemical Physics* **2004**, *121* (23), 12060-12066. DOI: 10.1063/1.1815296.

(38) Hu, Y.; Sinha, S. K.; Patel, S. Investigating Hydrophilic Pores in Model Lipid Bilayers Using Molecular Simulations: Correlating Bilayer Properties with Pore-Formation Thermodynamics. *Langmuir* **2015**, *31* (24), 6615-6631. DOI: 10.1021/la504049q.

(39) Awasthi, N.; Hub, J. S. Simulations of Pore Formation in Lipid Membranes: Reaction Coordinates, Convergence, Hysteresis, and Finite-Size Effects. *Journal of Chemical Theory and Computation* **2016**, *12* (7), 3261-3269. DOI: 10.1021/acs.jctc.6b00369.

(40) Hub, J. S.; Awasthi, N. Probing a Continuous Polar Defect: A Reaction Coordinate for Pore Formation in Lipid Membranes. *Journal of Chemical Theory and Computation* **2017**, *13* (5), 2352-2366. DOI: 10.1021/acs.jctc.7b00106.

(41) Roesel, D.; Eremchev, M.; Poojari, C. S.; Hub, J. S.; Roke, S. Ion-Induced Transient Potential Fluctuations Facilitate Pore Formation and Cation Transport through Lipid Membranes. *Journal of the American Chemical Society* **2022**, *144* (51), 23352-23357. DOI: 10.1021/jacs.2c08543.

(42) Kasparyan, G.; Poojari, C.; Róg, T.; Hub, J. S. Cooperative Effects of an Antifungal Moiety and DMSO on Pore Formation over Lipid Membranes Revealed by Free Energy Calculations. *The Journal of Physical Chemistry B* **2020**, *124* (40), 8811-8821. DOI: 10.1021/acs.jpcb.0c03359.

(43) Awasthi, N.; Kopec, W.; Wilkosz, N.; Jamróz, D.; Hub, J. S.; Zatorska, M.; Petka, R.; Nowakowska, M.; Kepczynski, M. Molecular Mechanism of Polycation-Induced Pore Formation in Biomembranes. *ACS Biomaterials Science & Engineering* **2019**, *5* (2), 780-794. DOI: 10.1021/acsbiomaterials.8b01495.

(44) Thøgersen, L.; Schiøtt, B.; Vosegaard, T.; Nielsen, N. C.; Tajkhorshid, E. Peptide Aggregation and Pore Formation in a Lipid Bilayer: A Combined Coarse-Grained and All Atom Molecular Dynamics Study. *Biophysical Journal* **2008**, *95* (9), 4337-4347. DOI: https://doi.org/10.1529/biophysj.108.133330.

(45) Kabelka, I.; Brožek, R.; Vácha, R. Selecting Collective Variables and Free-Energy Methods for Peptide Translocation across Membranes. *Journal of Chemical Information and Modeling* **2021**, *61* (2), 819-830. DOI: 10.1021/acs.jcim.0c01312.

(46) de Jong, D. H.; Singh, G.; Bennett, W. F. D.; Arnarez, C.; Wassenaar, T. A.; Schäfer, L. V.; Periole, X.; Tieleman, D. P.; Marrink, S. J. Improved Parameters for the Martini Coarse-Grained Protein Force Field. *Journal of Chemical Theory and Computation* **2013**, *9* (1), 687-697. DOI: 10.1021/ct300646g.

(47) Wassenaar, T. A.; Ingólfsson, H. I.; Böckmann, R. A.; Tieleman, D. P.; Marrink, S. J. Computational Lipidomics with insane: A Versatile Tool for Generating Custom Membranes for Molecular Simulations. *Journal of Chemical Theory and Computation* **2015**, *11* (5), 2144-2155. DOI: 10.1021/acs.jctc.5b00209.

(48) Hanwell, M. D.; Curtis, D. E.; Lonie, D. C.; Vandermeersch, T.; Zurek, E.; Hutchison, G. R. Avogadro: an advanced semantic chemical editor, visualization, and analysis platform. *Journal of Cheminformatics* **2012**, *4* (1), 17. DOI: 10.1186/1758-2946-4-17.

(49) Tribello, G. A.; Bonomi, M.; Branduardi, D.; Camilloni, C.; Bussi, G. PLUMED 2: New feathers for an old bird. *Computer Physics Communications* **2014**, *185* (2), 604-613. DOI: https://doi.org/10.1016/j.cpc.2013.09.018.

(50) Marrink, S. J.; Risselada, H. J.; Yefimov, S.; Tieleman, D. P.; de Vries, A. H. The MARTINI Force Field: Coarse Grained Model for Biomolecular Simulations. *The Journal of Physical Chemistry B* **2007**, *111* (27), 7812-7824. DOI: 10.1021/jp071097f.

(51) Michalowsky, J.; Schäfer, L. V.; Holm, C.; Smiatek, J. A refined polarizable water model for the coarse-grained MARTINI force field with long-range electrostatic interactions. *The Journal of Chemical Physics* **2017**, *146* (5), 054501. DOI: 10.1063/1.4974833.

(52) Souza, P. C. T.; Alessandri, R.; Barnoud, J.; Thallmair, S.; Faustino, I.; Grünewald, F.; Patmanidis, I.; Abdizadeh, H.; Bruininks, B. M. H.; Wassenaar, T. A.; et al. Martini 3: a general purpose force field for coarse-grained molecular dynamics. *Nature Methods* **2021**, *18* (4), 382-388. DOI: 10.1038/s41592-021-01098-3.

(53) Darden, T.; York, D.; Pedersen, L. Particle mesh Ewald: An N·log(N) method for Ewald sums in large systems. *The Journal of Chemical Physics* **1993**, *98* (12), 10089-10092. DOI: 10.1063/1.464397.

(54) Bussi, G.; Donadio, D.; Parrinello, M. Canonical sampling through velocity rescaling. *The Journal of Chemical Physics* **2007**, *126* (1), 014101. DOI: 10.1063/1.2408420.

(55) Berendsen, H. J. C.; Postma, J. P. M.; van Gunsteren, W. F.; DiNola, A.; Haak, J. R. Molecular dynamics with coupling to an external bath. *The Journal of Chemical Physics* **1984**, *81* (8), 3684-3690. DOI: 10.1063/1.448118.

(56) Wassenaar, T. A.; Pluhackova, K.; Böckmann, R. A.; Marrink, S. J.; Tieleman, D. P. Going Backward: A Flexible Geometric Approach to Reverse Transformation from Coarse Grained to Atomistic Models. *Journal of Chemical Theory and Computation* **2014**, *10* (2), 676-690. DOI: 10.1021/ct400617g.

(57) Di Bartolo, A. L.; Masone, D. Synaptotagmin-1 C2B domains cooperatively stabilize the fusion stalk via a master-servant mechanism. *Chemical Science* **2022**, *13* (12), 3437-3446, 10.1039/D1SC06711G. DOI: 10.1039/D1SC06711G.

(58) Di Bartolo, A. L.; Tomes, C. N.; Mayorga, L. S.; Masone, D. Enhanced Expansion and Reduced Kiss-and-Run Events in Fusion Pores Steered by Synaptotagmin-1 C2B Domains. *Journal of Chemical Theory and Computation* **2022**, *18* (7), 4544-4554. DOI: 10.1021/acs.jctc.2c00424.

(59) Caparotta, M.; Tomes, C. N.; Mayorga, L. S.; Masone, D. The Synaptotagmin-1 C2B Domain Is a Key Regulator in the Stabilization of the Fusion Pore. *Journal of Chemical Theory and Computation* **2020**, *16* (12), 7840-7851. DOI: 10.1021/acs.jctc.0c00734.

(60) Parrinello, M.; Rahman, A. Crystal Structure and Pair Potentials: A Molecular-Dynamics Study. *Physical Review Letters* **1980**, *45* (14), 1196-1199. DOI: 10.1103/PhysRevLett.45.1196.

(61) Grossfield, A. *"WHAM: an implementation of the weighted*

histogram analysis method". http://membrane.urmc.rochester.edu/content/wham/, (accessed 2024/02/07).

(62) López, C. A.; Zhang, X.; Aydin, F.; Shrestha, R.; Van, Q. N.; Stanley, C. B.; Carpenter, T. S.; Nguyen, K.; Patel, L. A.; Chen, D.; et al. Asynchronous Reciprocal Coupling of Martini 2.2 Coarse-Grained and CHARMM36 All-Atom Simulations in an Automated Multiscale Framework. *Journal of Chemical Theory and Computation* **2022**, *18* (8), 5025-5045. DOI: 10.1021/acs.jctc.2c00168.

(63) Ingólfsson, H. I.; Lopez, C. A.; Uusitalo, J. J.; de Jong, D. H.; Gopal, S. M.; Periole, X.; Marrink, S. J. The power of coarse graining in biomolecular simulations. *WIREs Computational Molecular Science* **2014**, *4* (3), 225-248. DOI: https://doi.org/10.1002/wcms.1169.

(64) Filippov, A.; Orädd, G.; Lindblom, G. The effect of cholesterol on the lateral diffusion of phospholipids in oriented bilayers. *Biophys J* **2003**, *84* (5), 3079-3086. DOI: 10.1016/s0006-3495(03)70033-2.

(65) Ambroggio, E. E.; Separovic, F.; Bowie, J. H.; Fidelio, G. D.; Bagatolli, L. A. Direct Visualization of Membrane Leakage Induced by the Antibiotic Peptides: Maculatin, Citropin, and Aurein. *Biophysical Journal* **2005**, *89* (3), 1874-1881. DOI: https://doi.org/10.1529/biophysj.105.066589.

(66) Praporski, S.; Mechler, A.; Separovic, F.; Martin, L. L. Subtle Differences in Initial Membrane Interactions Underpin the Selectivity of Small Antimicrobial Peptides. *ChemPlusChem* **2015**, *80* (1), 91-96. DOI: https://doi.org/10.1002/cplu.201402318.

(67) Miyazaki, Y.; Shinoda, W. Cooperative antimicrobial action of melittin on lipid membranes: A coarse-grained molecular dynamics study. *Biochimica et Biophysica Acta (BBA) - Biomembranes* **2022**, *1864* (9), 183955. DOI: https://doi.org/10.1016/j.bbamem.2022.183955.

(68) Sun, D.; Forsman, J.; Woodward, C. E. Multistep Molecular Dynamics Simulations Identify the Highly Cooperative Activity of Melittin in Recognizing and Stabilizing Membrane Pores. *Langmuir* **2015**, *31* (34), 9388-9401. DOI: 10.1021/acs.langmuir.5b01995.

(69) Hirsh, D. J.; Hammer, J.; Maloy, W. L.; Blazyk, J.; Schaefer, J. Secondary Structure and Location of a Magainin Analogue in Synthetic Phospholipid Bilayers. *Biochemistry* **1996**, *35* (39), 12733-12741. DOI: 10.1021/bi961468a.

(70) Matsuzaki, K.; Murase, O.; Tokuda, H.; Funakoshi, S.; Fujii, N.; Miyajima, K. Orientational and Aggregational States of Magainin 2 in Phospholipid Bilayers. *Biochemistry* **1994**, *33* (11), 3342-3349. DOI: 10.1021/bi00177a027.

(71) Karal, M. A. S.; Alam, J. M.; Takahashi, T.; Levadny, V.; Yamazaki, M. Stretch-Activated Pore of the Antimicrobial Peptide, Magainin 2. *Langmuir* **2015**, *31* (11), 3391-3401. DOI: 10.1021/la503318z.

(72) Han, M.; Mei, Y.; Khant, H.; Ludtke, S. J. Characterization of Antibiotic Peptide Pores Using Cryo-EM and Comparison to Neutron Scattering. *Biophysical Journal* **2009**, *97* (1), 164-172. DOI: https://doi.org/10.1016/j.bpj.2009.04.039.

(73) Marrink, S. J.; Monticelli, L.; Melo, M. N.; Alessandri, R.; Tieleman, D. P.; Souza, P. C. T. Two decades of Martini: Better beads, broader scope. *WIREs Computational Molecular Science* **2023**, *13* (1), e1620. DOI: https://doi.org/10.1002/wcms.1620.

(74) Saeedimasine, M.; Montanino, A.; Kleiven, S.; Villa, A. Role of lipid composition on the structural and mechanical features of axonal membranes: a molecular simulation study. *Scientific Reports* **2019**, *9* (1), 8000. DOI: 10.1038/s41598-019-44318-9.

(75) Hub, J. S. Joint Reaction Coordinate for Computing the Free-Energy Landscape of Pore Nucleation and Pore Expansion in Lipid Membranes. *Journal of Chemical Theory and Computation* **2021**, *17* (2), 1229-1239. DOI: 10.1021/acs.jctc.0c01134.

(76) Naito, A.; Nagao, T.; Norisada, K.; Mizuno, T.; Tuzi, S.; Saitô, H. Conformation and Dynamics of Melittin Bound to Magnetically Oriented Lipid Bilayers by Solid-State 31P and 13C NMR Spectroscopy. *Biophysical Journal* **2000**, *78* (5), 2405-2417. DOI: https://doi.org/10.1016/S0006-3495(00)76784-1.

(77) Yang, L.; Harroun, T. A.; Weiss, T. M.; Ding, L.; Huang, H. W. Barrel-Stave Model or Toroidal Model? A Case Study on Melittin Pores. *Biophysical Journal* **2001**, *81* (3), 1475-1485. DOI: https://doi.org/10.1016/S0006-3495(01)75802-X.

(78) Verbeek, S. F.; Awasthi, N.; Teiwes, N. K.; Mey, I.; Hub, J. S.; Janshoff, A. How arginine derivatives alter the stability of lipid membranes: dissecting the roles of side chains, backbone and termini. *European Biophysics Journal* **2021**, *50* (2), 127-142. DOI: 10.1007/s00249-021-01503-x.

(79) Rocha-Roa, C.; Orjuela, J. D.; Leidy, C.; Cossio, P.; Aponte-Santamaría, C. Cardiolipin prevents pore formation in phosphatidylglycerol bacterial membrane models. *FEBS Letters* **2021**, *595* (21), 2701-2714. DOI: https://doi.org/10.1002/1873-3468.14206.

(80) Tachi, T.; Epand, R. F.; Epand, R. M.; Matsuzaki, K. Position-Dependent Hydrophobicity of the Antimicrobial Magainin Peptide Affects the Mode of Peptide−Lipid Interactions and Selective Toxicity. *Biochemistry* **2002**, *41* (34), 10723-10731. DOI: 10.1021/bi0256983.

(81) Ludtke, S. J.; He, K.; Heller, W. T.; Harroun, T. A.; Yang, L.; Huang, H. W. Membrane Pores Induced by Magainin. *Biochemistry* **1996**, *35* (43), 13723-13728. DOI: 10.1021/bi9620621.

(82) Sun, D.; Forsman, J.; Woodward, C. E. Molecular Simulations of Melittin-Induced Membrane Pores. *The Journal of Physical Chemistry B* **2017**, *121* (44), 10209-10214. DOI: 10.1021/acs.jpcb.7b07126.

(83) Sun, D.; Forsman, J.; Woodward, C. E. Amphipathic Membrane-Active Peptides Recognize and Stabilize Ruptured Membrane Pores: Exploring Cause and Effect with Coarse-Grained Simulations. *Langmuir* **2015**, *31* (2), 752-761. DOI: 10.1021/la5038266.

(84) Mihajlovic, M.; Lazaridis, T. Antimicrobial peptides in toroidal and cylindrical pores. *Biochimica et Biophysica Acta (BBA) - Biomembranes* **2010**, *1798* (8), 1485-1493. DOI: https://doi.org/10.1016/j.bbamem.2010.04.004.

(85) Cheraghi, N.; Hosseini, M.; Mohammadinejad, S. Pore formation and the key factors in antibacterial activity of aurein 1.2 and LLAA inside lipid bilayers, a molecular dynamics study. *Biochimica et Biophysica Acta (BBA) - Biomembranes* **2018**, *1860* (2), 347-356. DOI: https://doi.org/10.1016/j.bbamem.2017.10.009.

(86) Piggot, T. J.; Allison, J. R.; Sessions, R. B.; Essex, J. W. On the Calculation of Acyl Chain Order Parameters from Lipid Simulations. *Journal of Chemical Theory and Computation* **2017**, *13* (11), 5683-5696. DOI: 10.1021/acs.jctc.7b00643.

(87) Beschiaschvili, G.; Seelig, J. Melittin binding to mixed phosphatidylglycerol/phosphatidylcholine membranes. *Biochemistry* **1990**, *29* (1), 52-58. DOI: 10.1021/bi00453a007.

(88) Harmouche, N.; Bechinger, B. Lipid-Mediated Interactions between the Antimicrobial Peptides Magainin 2 and PGLa in Bilayers. *Biophysical Journal* **2018**, *115* (6), 1033-1044. DOI: https://doi.org/10.1016/j.bpj.2018.08.009.

(89) Grage, S. L.; Afonin, S.; Kara, S.; Buth, G.; Ulrich, A. S. Membrane Thinning and Thickening Induced by Membrane-Active Amphipathic Peptides. *Front Cell Dev Biol* **2016**, *4*, 65. DOI: 10.3389/fcell.2016.00065.

(90) Bhat, R.; Foster, L. L.; Rani, G.; Vemparala, S.; Kuroda, K. The function of peptide-mimetic anionic groups and salt bridges in the antimicrobial activity and conformation of cationic amphiphilic copolymers. *RSC Advances* **2021**, *11* (36), 22044-22056, 10.1039/D1RA02730A. DOI: 10.1039/D1RA02730A.

(91) Marqusee, S.; Baldwin, R. L. Helix stabilization by Glu-...Lys+ salt bridges in short peptides of de novo design. *Proc Natl Acad Sci U S A* **1987**, *84* (24), 8898-8902. DOI: 10.1073/pnas.84.24.8898.

(92) Walther, T. H.; Ulrich, A. S. Transmembrane helix assembly and the role of salt bridges. *Current Opinion in Structural Biology* **2014**, *27*, 63-68. DOI: https://doi.org/10.1016/j.sbi.2014.05.003.

(93) Zerweck, J.; Strandberg, E.; Kukharenko, O.; Reichert, J.; Bürck, J.; Wadhwani, P.; Ulrich, A. S. Molecular mechanism of synergy between the antimicrobial peptides PGLa and magainin 2. *Scientific Reports* **2017**, *7* (1), 13153. DOI: 10.1038/s41598-017-12599-7.

(94) Dufourc, E. J.; Smith, I. C.; Dufourcq, J. Molecular details of melittin-induced lysis of phospholipid membranes as revealed by deuterium and phosphorus NMR. *Biochemistry* **1986**, *25* (21), 6448-6455. DOI: 10.1021/bi00369a016.

(95) Sandre, O.; Moreaux, L.; Brochard-Wyart, F. Dynamics of transient pores in stretched vesicles. *Proceedings of the National Academy of Sciences* **1999**, *96* (19), 10591-10596. DOI: 10.1073/pnas.96.19.10591.

(96) Levadny, V.; Tsuboi, T.-a.; Belaya, M.; Yamazaki, M. Rate Constant of Tension-Induced Pore Formation in Lipid Membranes. *Langmuir* **2013**, *29* (12), 3848-3852. DOI: 10.1021/la304662p.

(97) Hasan, M.; Karal, M. A. S.; Levadnyy, V.; Yamazaki, M. Mechanism of Initial Stage of Pore Formation Induced by Antimicrobial Peptide Magainin 2. *Langmuir* **2018**, *34* (10), 3349-3362. DOI: 10.1021/acs.langmuir.7b04219.

TOC Graphic